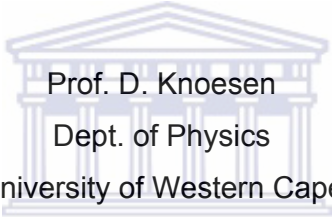


**AN INVESTIGATION INTO THE ROLE OF HYDROGEN EMBRITTLEMENT  
IN THE FORMATION OF SPLIT BODIES IN TWO-PIECE FOOD CANS**

Thesis presented in fulfillment of the requirements for the degree of Master of  
Sciences at the University of Western Cape by

Fakhree Majiet

Supervisor:



Prof. D. Knoesen  
Dept. of Physics  
University of Western Cape

Co-supervisor:

Dr. M. Maluleke  
Corrosion and Surface Studies  
Nampak R&D

**March 2009**



**DECLARATION**

I, the undersigned, hereby declare that the work contained in this thesis is my own original work and that I have not previously in its entirety or in part submitted it at any university for a degree and that I have not previously submitted it in its entirety or in part to any other university for a degree.

Signature: .....

Date: .....





## **ABSTRACT**

Nampak packages millions of cans a year and a very small percentage of these cans fail due to many reasons. One of the main reasons that cause 2-piece food cans to fail is split flanges. Split Flanges arises due to a number of reasons which will be discussed in detail.

The focus of this thesis was based on the causes of split flanges in 2-piece food cans. A study on manufacturing the steel and can making together with packaging fish in these cans was conducted. Another study on the reasons for split flanges occurring in 2 piece cans was conducted done as well.

The purpose of the investigation was to check if hydrogen embrittlement could be the cause for split bodies forming in 2 piece food cans. 2 piece cans are drawn and wall ironed from tinplate; the cans were made up of a top and a shaped body. It was this shaped body that went through a considerable amount of stress during manufacture especially at the top of the can, which gave an explanation to why the cans split at the curved area near the flange of the can.

According to previous studies done at Nampak R&D more complaints about split bodies were coming from the Fish canneries on the West Coast than the Vegetable canneries. These canneries used the exact same cans to package their product. The difference between the processes at these canneries was the exhaust boxes at the fish canneries. The exhaust box is a long tunnel filled with steam used to precook the fish; the vegetables are not precooked in exhaust boxes. Non metallic inclusions (NMI) was one of the main reason for these split flanges to occur and a reason of particular interest in this research. NMI's were distributed throughout the steel of the cans and since the same cans were used for the fish and vegetable canneries, they should be failing at the same rate. Yet only complaints came from the fish canneries. So the primary focus of the research was to check if the additional steam process contributed to the formation of split bodies / flanges. We proposed to investigate if hydrogen atoms collect at grain boundaries, vacancies and non metallic inclusions and also to check if the steam accelerated embrittlement.

Hydrogen is believed to penetrate right into the bare steel of the cans that were exposed to steam.

Hydrogen atoms are being investigated because of their small size, their ability to diffuse through a metal lattice and form hydrogen molecules within the intermetallic vacancies of the metal. The molecules of hydrogen, once formed within the internal structure of the metal, remain trapped because of their larger size and can generate a significant pressure that can contribute to the formation of split bodies. [1]

The first step to prove whether H-embrittlement was present in the cans was to check if hydrogen was present. A spectroscopic method namely, elastic recoil detection analysis (ERDA) was used to check if H could be detected using the Elastic Recoil Detection Analysis technique. Several experiments were designed to make sure the technique was suitable for the detection of H. Even though it is known that all metals are susceptible to corrosion and H-embrittlement, the tinplate metals had to be checked in an environment similar to the exhaust box (suspected area causing hydrogen embrittlement) in the factories.

Further characterization was done using X-Ray Diffraction to measure the residual stress and relate it to the effects of H-embrittlement. If the H had penetrated into the metal it would cause some distortion in the atomic distances between the atomic planes in Fe atoms and can be measured using XRD.

Another effect of hydrogen embrittlement is to reduce the strength in the metal. Tensile tests were performed to measure the strengths of the metal.

## **ACKNOWLEDGEMENTS**

It is hard for me to express all the gratitude for all the individuals that have helped me throughout my university career. Hopefully I can share some of the appreciation in the next few pages.

I would like to thank my supervisor Prof. Dirk Knoesen for his patience on this project and making things very easy with the collaboration with Nampak R&D. Prof allowed a lot of freedom for research, but supplied enough supervision to keep the project on task.

I would like to thank Nampak R&D for providing me with the opportunity to explore my research in such a worker friendly environment and for helping me to experience industrial research outside university. I have learnt so much concerning my project even much more that does not concern the project.

I would like to thank my co super-visor Dr. Mkhethwa Maluleke and Mr. Charles Hepburn at Nampak R&D for their input in to the project and the many useful discussions pertaining to the project.

I would like to thank Mr. R Davis for valuable lessons on steel making and metallurgy and the access to previous studies done at Nampak which made my research much easier.

I would like to thank the rest of the staff at Nampak R&D for helping me in their respective labs when ever I was there.

I would like to thank the University of the Western Cape for being a great institution. I have been at UWC for 5 years and turned out to be a spectacular experience for me.

I would like to thank Mr. Ian Schroeder and all the other staff in the physics building.

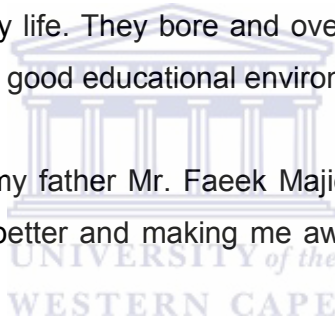
I would like to thank all my class mates for the great discussions we had. We always kept motivating each other to do better which certainly helped me.

I would like to thank iThemba LABS for doing ERDA measurement. And thanks to Phillip Sechonyona who always helped me around at iThemba.

I would like to thank NECSA for allowing me to use the XRD machine where I did residual stress analysis. And thanks to Tshepo Ntsoane together with Dr. Andrew Venter that made it possible for me to do the measurements at NECSA

Finally I would like to thank my parents and family for their support and who trusted me through out my life. They bore and overcame lots of difficulties in order to provide me with a good educational environment.

And a special thanks to my father Mr. Faeek Majiet who always pushed me and motivated me to do better and making me aware of matters around the world.





# **CONTENTS**

<b>CHAPTER 1</b>	<b><i>Introduction</i></b>	<b>1</b>
1.1	Background on H-embrittlement	1
1.2	Mechanism of Embrittlement of Steel by Hydrogen	2
<b>CHAPTER 2</b>	<b><i>Tinplate</i></b>	<b>5</b>
2.1	Historical background	5
2.2	Manufacturing the tinplate	5
2.3	The structure of tinplate	9
2.4	2 piece can making	11
2.5	Split bodies in 2-piece food cans	15
<b>CHAPTER 3</b>	<b><i>Analytical Techniques</i></b>	<b>24</b>
3.1	Elastic Recoil Detection Analysis	24
3.2	Stress Analysis by XRD	42
3.3	Tensile Testing	55
<b>CHAPTER 4</b>	<b><i>Experimental Procedure</i></b>	<b>57</b>
<b>CHAPTER 5</b>	<b><i>Results and Discussion</i></b>	<b>60</b>
	<b><i>Conclusion</i></b>	<b>85</b>
	<b><i>Reference</i></b>	<b>86</b>

## **LIST OF TABLES AND FIGURES**

Figure 2-1: Continuous casting of steel. [2.1].....	6
Figure 2-2: Hot rolling of steel and the effect on grain structure. [2.1] .....	7
Figure 2-3: A low carbon sheet steel in the (a) as cold rolled unannealed condition, (b) partially recrystallized annealed condition, and (c) fully recrystallised annealed condition. [2.1] .....	8
Figure 2-4: The layered structure of tin free steel and tinplate. ....	9
Figure 2-5: A split flange that occurs immediately after the cans are seamed. [2.2] .....	15
Figure 2-7: A micrographs of Non-Metallic Inclusions in the (Split) Flange of a Can. [2.1] Sizes of the indicated NMIs (from Left to Right) are $65\mu$ , $55\mu$ and $175\mu$ . [2.1] .....	17
Figure 2-8: A typical EDS spectrum highlighting which elements the NMI was made of. [2] .....	18
Figure 2-9: A spiral trim. [2.1].....	19
Figure 2-10: A stepped can. [2.1]3) Can (Flange) Damage .....	19
3) Can (Flange) Damage .....	20
Figure 2-11: Damaged flange. [2.1].....	20
Figure 2-12: Damaged flange. [2.1].....	20
Figure 2-13: Damaged flange. [2.1].....	21
Figure 2-14: Damage caused by peening. [2.1] .....	22
Figure 2-15: damage caused by peening. [2.1] .....	22
Figure 2-16: The flow of metal into the characteristic mushroom shape. [2.1] .....	23
Figure 3-1: Schematic representation of a classical geometry of a scattering experiment in the laboratory frame of reference. Left is before and right is after the scattering event. [3.6] .....	27
Figure 3-2: Recoils scattered from the surface have energy $E_2$ , while recoils scattered from depth $t$ have energy $E_3$ , the $x$ -axis is perpendicular to the surface of the sample. [3.5].....	30
Figure 3-3: Geometry of a scattering experiment. Incident angle $\alpha$ , exit angle $\beta$ and scattering angle $\theta$ . [3.8].....	33
Figure 3-4: The spectrum from a kapton reference sample bombarded by 2 MeV He <sup>++</sup> projectiles.....	35
Figure 3-5: The spectrum from a kapton reference sample bombarded by 2.5 MeV He <sup>++</sup> projectiles.....	35
Figure 3-6: The spectrum from a kapton reference sample bombarded by 3 MeV He <sup>++</sup> projectiles.....	36
Table 3-1: Data for energy calibration.....	36
Figure 3-7: Energy-channel calibration experiment; the three points shown on the graph correspond to 3 calculated detected energies from an initial beam of 2, 2.5 and 3 MeV respectively.....	36
Figure 3-8: The simulated ERDA spectrum at 3 MeV.....	37
Table 3-2: Molar Mass details for Mylar foil.....	38
Table 3-3: Molar Mass details for Kapton standards.....	38
Figure 3-9: The disc on the left is a tinplate sheet before it gets drawn into the can on the right.....	39
Table 3-5: Molar Mass details for FeSn <sub>2</sub> layer in the can. ....	41
Figure 3-10: Diffractometer scheme. [3.10].....	42
The incident beam diffracts X-rays of wavelength $\lambda$ from planes which satisfy Bragg's law. If the surface is in compression then the planes are closer together than in the stress-free state because of Poisson's ratio. The interplanar spacing $d$ is obtained from the peak in intensity versus scattering angle and Bragg's law [3.10].....	43
Figure 3-11: When the sample is tilted, diffraction will take place from other grains, but from the same planes (that satisfy Bragg's law). The peak takes place at higher values of $2\theta$ . [3.10] .....	43
Figure 3-12: Diffraction of x-rays by a crystal and Bragg's law [3.11] .....	46
Figure 3-13: An x-ray diffractometer scheme [3.10].....	47
Figure 3-14: Sample and laboratory coordinate systems. [3.10].....	49
Figure 3-15: The geometric definition of diffraction rings in laboratory axes. [3.11] .....	51
Figure 3-16: The relationship between the three spaces and the laboratory coordinates. [3.12].....	52
Figure 3-17: The measured biaxial stress tensor and pseudo hydrostatic stress as a function of input $d_p$ . [3.11] .....	53
Figure 3-18: The diffracted rings detected by a 2D detector .....	54
Figure 3-19: Red point focusing on the sample using the video alignment system .....	54
Figure 3-20: All the factors involved in a Stress Strain graph.....	56
Table 2: Measurement details from the Brukers Leptos v6 software:.....	58
Figure 5-1: A simulated ERDA spectrum for a sample with no H treatment. ....	60
Figure 5-2: A simulated ERDA spectrum for the sample exposed to steam only. ....	61

<i>Figure 5-3: A simulated ERDA spectrum for the sample exposed to steam and acid</i> .....	61
<i>Figure 5-4: A simulated ERDA spectrum for the sample exposed to steam and fish</i> .....	62
<i>Figure 5-5: A comparison of two ERDA spectra for different samples with no H treatment</i> .....	63
<i>Figure 5-6: A comparison of two ERDA spectra for different samples treated with steam and product</i> .....	63
<i>Figure 5-7: A comparison of the ERDA spectra for differently prepared samples with no protection</i> .	64
<i>Figure 5-8: A close up on the ERDA spectrum for differently prepared samples with different treatment</i> .....	65
<i>Figure 5-9: A depth profiling curve for differently prepared samples with no lacquer protection</i> .....	66
<i>Figure 5-10: Quantitative analysis of the average hydrogen concentrations for different H treatments</i> .....	67
<i>Figure 5-11: A comparison of the ERDA spectra for differently prepared samples protected with lacquer protection</i> .....	68
<i>Figure 5-12: A close up ERDA spectrum of the comparison for differently prepared samples</i> .....	69
<i>Figure 5-13: A depth profiling curve for differently prepared samples with lacquer protection</i> .....	70
<i>Figure 5-14: A quantitative analysis of the hydrogen concentration throughout the sample and in the steel matrix of the protected samples</i> .....	70
<i>Figure 5-15: Phase Analysis for a tinplate sample</i> .....	72
<i>Figure 5-16: Images of the diffracted beam at different sample tilts for 2D XRD</i> .....	73
<i>Table 5-4: Residual Stress data for 3 different stress orientations and all the respective treatments using the Cu tube</i> .....	74
<i>Table 5-5: Average Residual Stresses measured with the Cu tube for the respective treatments</i> .....	75
<i>Figure 5-17: Average Residual Stress measurements for the respective treatments with a Cu tube</i> .....	75
<i>Figure 5-18: The signal to noise ratio for the Cu tube</i> .....	76
<i>Figure 5-19: The signal to noise ratio for the Co tube</i> .....	77
<i>Table 5-6: Residual Stress data for 3 different stress orientations and all the respective treatments with the Co tube</i> .....	78
<i>Table 5-7: Average Residual Stress measurements for the respective treatments with the Co tube</i> .....	78
<i>Figure 5-20: Average Residual Stress measurements for the respective treatments using the Co tube</i> .....	79
<i>Table 5-9: Samples exposed to steam only</i> .....	81
<i>Figure 5-21: Average tensile stresses for differently prepared samples</i> .....	82



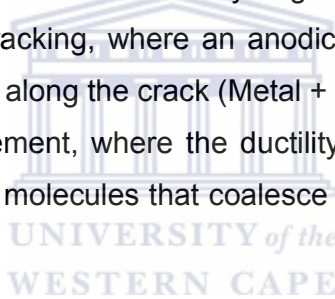
# CHAPTER 1 INTRODUCTION

## 1.1 Background on H-embrittlement

The degradation of materials is of great importance to any builder, designer and operator of structures made of metals. The damages can cause a loss in reliability, a reduction in safety and increased costs due to additional maintenance, higher down time or replacement of failed components.

The extent of hydrogen damage is not known to the general public and the reduced visual appearance results in greater effort for detection. Three different mechanisms can be attributed to the degradation of a material in which hydrogen plays a role:

1. Surface corrosion with formation of hydrogen-compounds,
2. Stress corrosion cracking, where an anodic dissolution with formation of hydrogen occurs along the crack ( $\text{Metal} + \text{H}_2\text{O} > \text{Metal} (\text{OH})^- + \text{H}^+$ ),
3. Hydrogen Embrittlement, where the ductility of a metal is reduced by hydrogen atoms or molecules that coalesce in the granular structure of the metal.



Some examples where hydrogen causes damage in steel and the implications for the operation of the structure are given [1.1]:

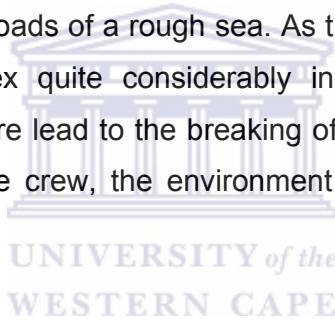
- The rusting of iron under atmospheric conditions in motor vehicles. Many cars are taken out of service due to this kind of corrosion or hydrogen damage while other mechanical parts are still in good condition.

- Petrochemical Industries contain hundreds of kilometers of pipes and a multitude of reaction vessels. These can contain hydrocarbon-compounds at high temperature and pressure. The combination of the transported fluid and physical properties makes the materials used for construction very susceptible to hydrogen degradation. The pipes are often very long and due to temperature and pressure changes have to possess a certain degree of flexibility. A brittle region in a pipe is thus a potential breaking point. Pipe breaks can lead to large production losses, the bursting of a reaction vessel

has the potential for serious risk to life and the environment. Hydrogen embrittlement can be caused by dissociation of the water/steam or, in a smaller extent, by H<sub>2</sub>-gas dissolved in the water. This is similar to the exhaust box in the canning factories where the cans are put through.

- Corrosion is caused by hydrate formation in aircrafts between two riveted plates which weakens the stability of the aircraft. Due to strict regulations put in place by the aviation industry, aeroplanes are taken out of service until repairs are done.

- The most common form of environmental attack on sea must be during ship building. Stress Corrosion Cracking (SCC) occurs in heat affected zones around welds, while hydrogen embrittlement can occur anywhere in the structure. Loss of ductility due to embrittlement seriously impairs the capability of the ship to absorb the loads of a rough sea. As these large vessels can not ride the waves, they flex quite considerably in a rough sea. Hydrogen embrittlement can therefore lead to the breaking of parts of the structure with catastrophic results to the crew, the environment and profit margins of the ships owner.



## **1.2 Mechanism of Embrittlement of Steel by Hydrogen**

In general the deformation of metals occurs by means of movement of dislocations along certain preferred directions (slip directions) within the individual crystals of the metal. Under these conditions, the moving dislocations tend to accumulate at barriers, such as grain boundaries or hard precipitate particles situated at the end of slip plains. Such an accumulation of dislocations can then lead to the formation of an embryo micro crack and/or intensive local stress concentration. These stresses can activate a neighboring set of dislocations (slip system), however, the harder the material and the lower the temperature, the higher the stress has to be to initiate this effect. Consequently, these high stresses can lead to the formation of micro cracks. The result of this is that the metal fractures in a brittle manner, after having sustained only a very small amount of plastic deformation.

Temperature plays an important role in this mechanism, as the general resistance of a metal to plastic deformation is lower at higher temperature. The first type of brittle fracture is intergranular fracture which propagates around the grain boundaries of a polycrystalline material. The second is transgranular fracture which propagates across a particular plane within a crystal.

In any case, the fracture originates from the initiation of a micro-crack, which has been formed by the above mentioned accumulation of dislocations. Hence, any change in the stress concentration and the formation of micro-cracks is likely to enhance the possibility of brittle-fracture. Hydrogen embrittlement arises as the result of the formation of micro-cracks in hydrogen-containing materials. The formation of the micro-crack takes place in one of two ways:

- 1) The micro-crack forms due to severe internal strains caused by the stress induced formation of a local concentration of hydrogen in interstitial solution.
- 2) The micro-crack forms as a result of the embrittling effect of hydrogen-rich constituents within the grains or at the grain boundaries of metals (reaction of alloying components with hydrogen).

Stress induced formation of local concentrations of hydrogen in iron and steel can be explained with the trap binding energy of a defect in the crystalline structure of the metal. If the binding energy is larger than the lattice migration energy of hydrogen in iron, hydrogen gets caught in the trap sites. There are four categories of traps:

- 1) Point defects with weak interactions. Some trapping of hydrogen occurs, however, only enough to influence but not enough to control hydrogen embrittlement.
- 2) Point defects with moderate to strong interactions. Larger amounts of hydrogen are trapped, having a stronger influence on embrittlement.
- 3) Dislocations with moderate to strong interactions. The influence on embrittlement is similar in magnitude to 2.

## CHAPTER 1 Introduction

4) Grain boundaries, interfaces and surfaces with strong interactions. These are the strongest two dimensional traps in the structure of a metal and have the ability to absorb substantial amounts of hydrogen.





## **CHAPTER 2 TINPLATE**

### **2.1 HISTORICAL BACKGROUND**

Tinplate was first made in the 14th century in Bavaria, Germany, spreading through Europe where it was utilized for articles such as mugs, plates, lanterns, tinderboxes and candlesticks. At the time tinplate was made from iron hammered into sheet form and dipped into molten tin (hot dipping). The use of rolled iron in tinplate was first accomplished in South Wales, UK in the mid 1700's. Food was first canned in the early 1800's using handmade tinplate cans. The electrolytic tinning of tinplate was the next major achievement to be accomplished, in Germany in the early 1930's. Up until the mid 1960's, Hot Dipped tinplate was quite common and is still used in India today for a wide variety of uses. In Europe, a company in London still uses this method of tinning for gas meters. Nowadays, the tinplate used for sanitary cans is electrolytically tinned. [2.1]

### **2.2 MANUFACTURING THE TINPLATE**

The tinplate is manufactured by making use of a 7-step process as described below:

#### **1. Continuous casting of steel slab:**

After refining in a Basic Oxygen Furnace, molten steel is teemed from a 200 tonne ladle into a 100 tonne "tundish". Steel from the tundish is cast through two water cooled, open ended moulds to form one continuous "string" (Fig. 1).

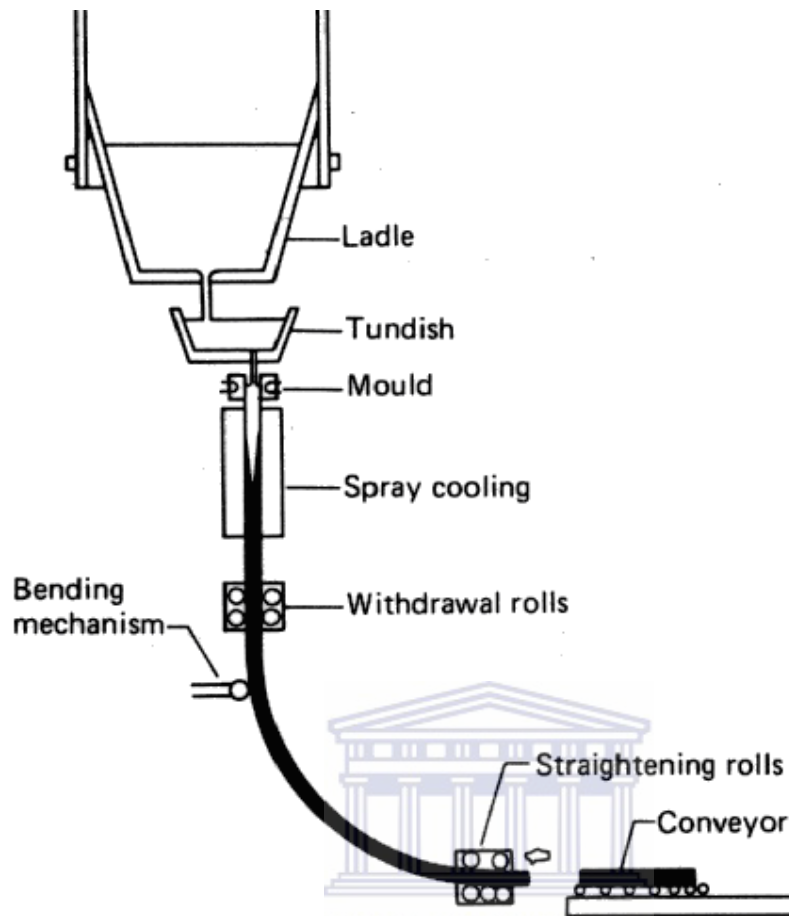


Figure 2-1: Continuous casting of steel. [2.1]

The continuous “strings” are flame cut into slabs, which are typically 300mm in thickness, 1250mm in width and 15m in length.

## 2. Hot Rolling:

The slabs are hot rolled from about 300mm thickness to about 2.0 – 2.5mm thickness, i.e. from slabs to coils. The rolling temperature starts at approximately 1150<sup>0</sup>C and ends at approximately 850<sup>0</sup>C. The length of such a coil is approximately 600m and this is coiled from strip at approximately 60km\hr. This breaks down the slab grain structure and reforms the grain. The type of grain and its size is governed in the “finishing section” of the hot rolling/coiling process. The rolled strip is coiled at approximately 600<sup>0</sup>C.

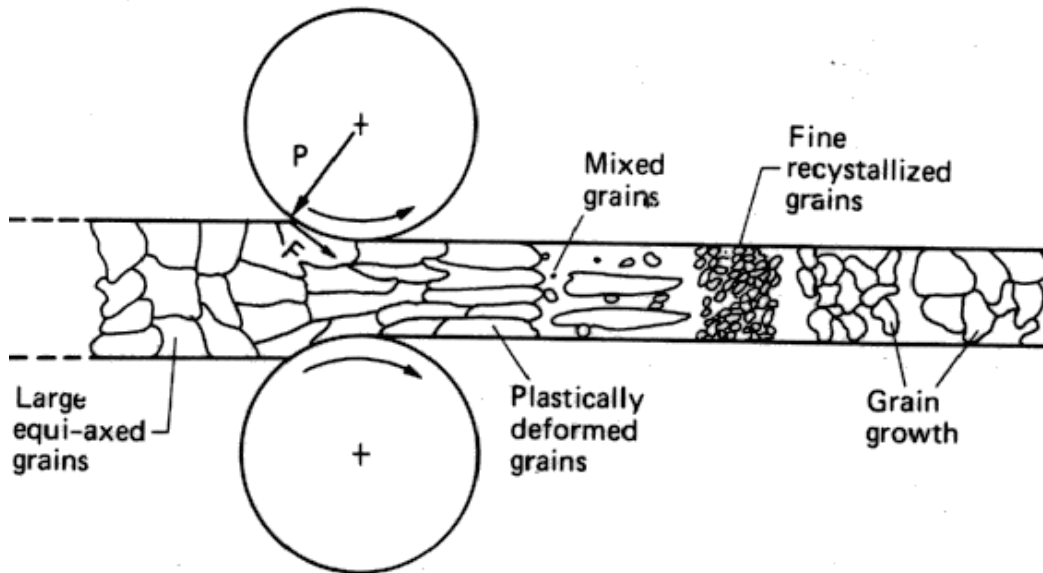


Figure 2-2: Hot rolling of steel and the effect on grain structure. [2.1]

### 3. Pickling:

The hot rolled coil, after cooling to room temperature, is cleaned (pickled) in hydrochloric acid, rinsed, dried and then oiled. The purpose of this is to remove any surface imperfections caused during the hot rolling process.

### 4. Cold Reduction:

The clean strip is then cold rolled down to about 0.20 – 0.30 mm thickness using great volumes of coolant to keep the strip cold. (The strip temperature rises to over 200°C during the process but this is considered cold). This process increases the hardness and improves the surface appearance.

### 5. Annealing:

The coil is now very hard (work hardened) and must be annealed to soften it before further processing. Annealing can take place by two technologies – Continuous Annealing for 3-piece tinplate and Drawn With Iron (DWI) food can plate and Batch Annealing for DWI beverage tinplate.

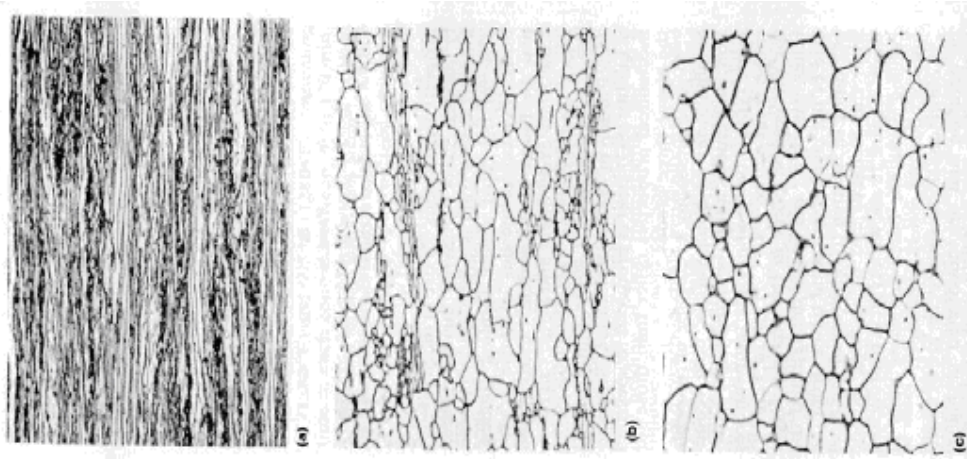


**Figure 2-3: A low carbon sheet steel in the (a) as cold rolled unannealed condition, (b) partially recrystallized annealed condition, and (c) fully recrystallized annealed condition. [2.1]**

The annealing process recrystallises the steel structure, ensuring that all previous distorted structures are obliterated.

#### 6. Tempering:

The strip is now very soft and needs to be hardened (Tempered) to the required, controlled degree for can making. Temper rolling gives the required strength, hardness, surface roughness and shape to the strip by reducing its thickness slightly and stretching it slightly between two rolls. In this case, the extension (stretch) of the strip is between 0.5 and 3% in length – depending on the required temper. This equates to a reduction in thickness of approximately the same amount.

#### 7. Electrolytic Tinning:

The next stage is to apply tin and this is carried out electrolytically in an Electrolytic Tinning Line (ETL). The lines are some 250m long and 40m in height and all the following process steps are carried out sequentially in such lines:

- a) The ETL's are of the Halogen type – using basic halide technology. In these lines, the strip is plated in a horizontal orientation and only one surface of the strip is plated at a time.

b) Flow melting is performed on the freshly tinned strip for 3-piece cans by heating the strip momentarily just above the melting point of tin and immediately freezing again. This forms the lustrous appearance and the alloy layer.

c) Passivation is then done in a sodium dichromate bath, either electrolytically passivation (for plate destined for food cans) or as a dip in passivation for plate destined for beverage cans.

d) Finally, Dioctyle sebacate (DOS) is applied in a mist through an electrostatic process. The strip passes between electrostatically charged wires that suspend the DOS mist. The strip is negatively charged and the mist is positively charged – the strip thus attracting the mist.

8. The completed coil is then re-coiled and packaged for dispatch to the can-maker.

### 2.3 THE STRUCTURE OF TINPLATE

Tinplate consists of four to five layers which are not always totally separate as they merge with one another:

1. Steel substrate
2. Tin coating
3. Free Tin and Alloyed Tin
4. Tin oxide (if present)
5. Protective layer

These layers can be ideally represented as in figure 2.4:

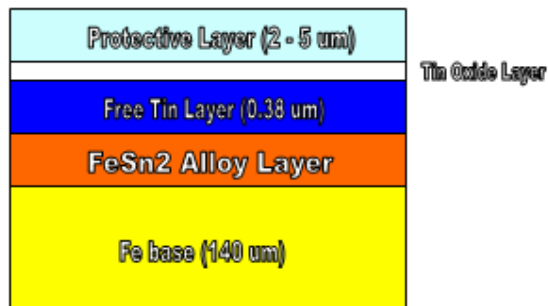


Figure 2-4: The layered structure of tin free steel and tinplate.

## CHAPTER 2 Tinplate

### 1. Steel Substrate

Steel is an alloy consisting predominantly of iron with less than 2 wt% carbon. The steel used in tinplate is similar to mild steel and has less than 0.12 wt% carbon. This carbon level is usually less than 0.08 wt% if the tinplate is used for welded can bodies.

2-piece cans are produced by the Drawn-and-Wall-Ironed (DWI) process. The forming processes are severe and require more stringent control over the steel properties. A higher degree of homogeneity, cleanliness, ductility, draw ability and low work hardening rate is required and carbon is usually maintained below 0.05 wt%. The microstructure contains grains with a density of up to 13 000 grains/mm<sup>2</sup>.

### 2. Tin Coating: Free Tin and Alloy Tin Layers

Depending on the application different masses of tin coating are used. Cans that are internally lacquered (meat, fish) require a lighter tin coating than cans containing fruit. The fruit in the latter cans reacts with the tin to retain its fresh appearance. This absorption of tin requires a much higher initial level of tin coating to provide the same protection. Certain can manufacturing processes may also require higher tin coatings for lubricity.

#### 2.1 Free Tin

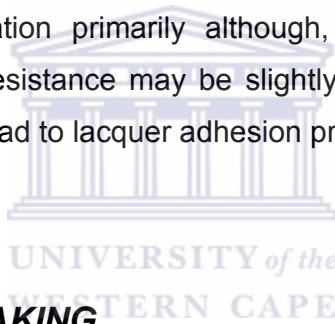
The free tin layer consists of pure tin, covering the surface of the tinplate. The most common low tin coating in South Africa is E1 (2.8\2.8 gm<sup>-2</sup>), i.e. the internal tin coating is 2.8 g.m<sup>-2</sup> and the external tin coating is 2.8 g.m<sup>-2</sup>. It provides a largely continuous coverage of the surface although thin spots and breaks in the layer ("pores") can be found. This is not necessarily a problem due to the presence of the alloy layer.

## 2.2 Alloy Layer:

The alloy layer consists of  $\text{FeSn}_2$  needle-like crystals. Ideally this layer would have a compact, dense structure to protect the underlying steel. In the event that both the free tin and alloy layer are broken and expose the steel, corrosion of the steel inside the can is minimised through galvanic protection. This is the same mechanism found in galvanized steel where the underlying steel is protected from corrosion by the preferential corrosion of the zinc coating. In the same way under anaerobic food can conditions the tin is anodic with respect to steel and will corrode preferentially, thereby protecting the steel.

## 3. Dioctyl Sebacate (DOS) Oil Layer

DOS is applied to the tinplate to provide lubricity for the manufacturing processes (sheet separation primarily although, on plain cans, beading, flanging) and corrosion resistance may be slightly aided. Exceeding a DOS level of  $\sim 10 \text{ mg/m}^2$  may lead to lacquer adhesion problems.



## **2.4 2 PIECE CAN MAKING**

The 2-piece can continuous production line is made up of the following process steps.

### 1. De-reeler

The  $\pm 10$  tonne coils are automatically unwound and fed through the inspection light and lubricator.

### 2. Lubricator

A thin film of drawing fluid is applied to both sides of the tinplate, to facilitate the metal forming process.

### 3. Cupping Press

Feed rollers “index” the plate into the cupping press at precisely the correct time and at exactly the right pitch, to present it to the two rows of tooling. The cupping press has a double action; the first action “blanks” out round discs and the second action draw the discs into shallow cups, approximately 96mm in diameter.

### 4. Body-makers

These are horizontal presses which perform the following steps on one cup-at-a-time, at up to 300 cans per minute

- Re draws the cup to 73mm diameter
- “Wall irons” the can once, reducing the wall thickness and increasing its height
- “Wall-irons” the can a second time, further reducing the wall thickness and increasing its height
- Forms the base profile of the can

In the body maker the tinsplate thickness is reduced from 0,31mm to 0,135mm at the mid wall area and 0,180mm at the top wall.

### 5. Trimmers

These machines trim off the rough edge of the cans leaving a can body of precisely the correct height.

### 6. Can Washer

The trimmed cans are covered in lubricant and therefore must be washed. They are conveyed upside down through the washer, on an open weave mat, approximately 2m wide. Inside the washer a caustic solution is sprayed onto and into the cans. The washing solution also contains a passivation chemical that prepares the surface for subsequent coating. Immediately after the chemical wash, the cans are rinsed clean with softened water and then with de-ionised water.

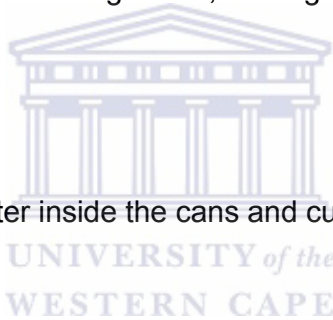


## 7. Wash Coater

After cleansing, the cans pass into the wash coater, where they are flooded with a wash-coat solution over the entire outside surface of the cans. The excess coating that remains in the inverted bases of the cans is blown out with an air jet.

## 8. Rim Dip

After a settling period, the cans are transferred by a magnetic conveyor, which lifts the cans by their bases and conveys them over a water bath. The excess coating that has accumulated around the open ends of the cans is removed by dipping the cans 5mm into the water. By the time that the cans have been transferred onto the drying oven mat, the remaining wash coat has flowed back over the flange area, leaving a thin film of coating over the whole can.



## 9. Drying Oven

The oven dries out the water inside the cans and cures the wash coat.

## 10. Flanger

Spin flanging is used to create the flange and to minimize the risk of split flanges.

## 11. Video inspection

A camera inspects the inside of each can to ensure that the trimmed-off portion of the can has not stuck inside the can. A can with a trim inside or with a dented body will be ejected from the conveyor into a scrap basket.

## CHAPTER 2 Tinline

### 12. Beader

Beading is carried out in a 16 head machine, where the roll-bead is also created. The roll-bead increases the strength of the lower wall of the can and also assists in the can handling.

### 13. Light tester

The tester is used to reject any cans with pinholes or split flanges.

### 14. Coding

A Video-jet machine prints the day/date and time on each can.

### 15. Internal spray machines

These machines spray a water based lacquer onto the inside surface of the can whilst they are spinning at high speed. In this way an even layer of coating is applied to the entire inner surface of the cans.

### 16. Internal Bake Oven

The cans are conveyed; open-end-up through a wide oven in which the water-based lacquer is dried and cured.

### 17. Inspection Station

Here cans are removed for Enamel rating, to check internal coating integrity and for immersion into copper sulphate to check the external coating.

### 18. Palletiser

A semi-automatic palletiser is used to form the pallets. At this point, outgoing Inspection is carried out on 30 cans from each pallet.

## 19. Strappers

Two strappers are used in order to apply at 2 x 3 strap configuration on each pallet: This is required in order to prevent movement of the cans during transit.

### ***2.5 Split Bodies in 2-piece food cans***



Figure 2-5: A split flange that occurs immediately after the cans are seamed. [2.2]

#### **Causes of Split Flanges / Bodies**

This problem can be caused at the steel maker, can maker, during transport to the can filler or at the can filler. Many reasons have been assigned to the causes of split flanges such as the presence of non metallic inclusions caused by the steel makers, peening caused by the cans vibrating against each other during transportation in trucks, trimming defects caused by the can makers during manufacture, excess material on the can bodies etc. and still there are a number of cases that have no explanation assigned to the cause of a split flange. Each of these problems will be discussed in this section together with the proposal for H-embrittlement as a cause for can failure.

### **1. Non Metallic Inclusions (NMIs) Caused at the Steel Makers.**

This is by far the greatest cause of split flanges \ bodies. The term is self explanatory and these are small particles of non-metallic compounds (usually oxides) which have been accidentally included in the steel.

NMI's usually originate at the steel making section of the steel works and come from the refractories used to cast the molten steel. Refractories are used throughout the steel making process to contain the heat of the molten or red-hot metal within a steel furnace or its associated casting processes by usually lining the carrying vessels similar to bricks in a wall. In the continuous casting process – such as that used to manufacture the steel from which tinsplate for DWI cans is made – refractory powders are also used to cover the surface of the molten steel to prevent oxidation of the steel. Other refractories are used for the nozzles through which the molten steel is teemed (poured) into the moulds. All these refractories become worn away slowly because molten steel is very abrasive. These become dissolved into the steel. Some of the refractory powder floating on top of the molten steel can also become entrapped and dissolve into the molten steel. All these become “NMIs” as they are not metallic.

During the subsequent rolling processes to manufacture tinsplate, the NMIs become dispersed throughout the steel. From any one cast slab, the final coil length is approximately 10 000m and its width is 936mm and the NMIs will be dispersed throughout this area. Should one or several compounded NMIs occur in the top wall of the finished ironed can (i.e. where the flange will be turned) then a split flange will result. This is because the NMI weakens the steel at that point where it occurs. The can is then rejected from the production process by light testers.

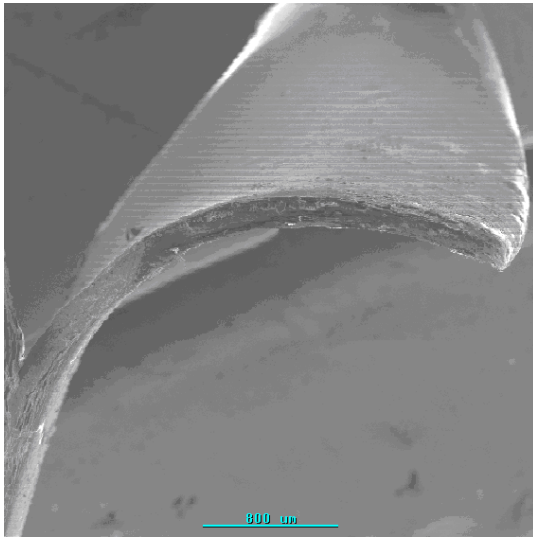


**Figure 2-6: A micrographs of Non-Metallic Inclusions in the (Split) Flange of a Can: These particles are very small – ranging from 10 - 200 $\mu$  in size. [2.1]**

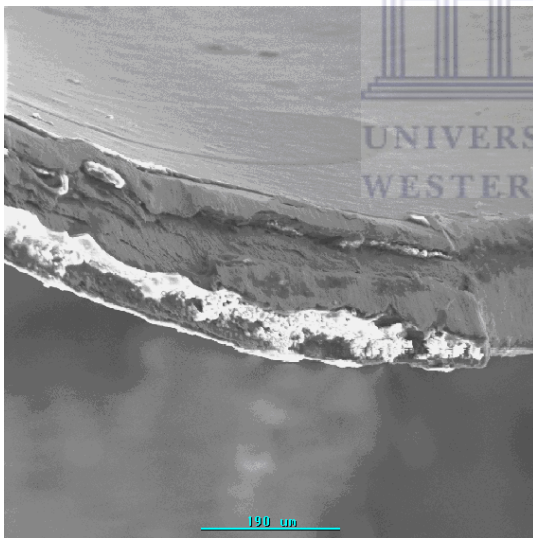


**Figure 2-7: A micrographs of Non-Metallic Inclusions in the (Split) Flange of a Can. [2.1] Sizes of the indicated NMIs (from Left to Right) are 65 $\mu$ , 55 $\mu$  and 175 $\mu$ . [2.1]**

(In this case, the NMIs are an aluminium \ calcium oxide rich complex as indicated in the analysis spectrum below – probably sourced during steel casting.)

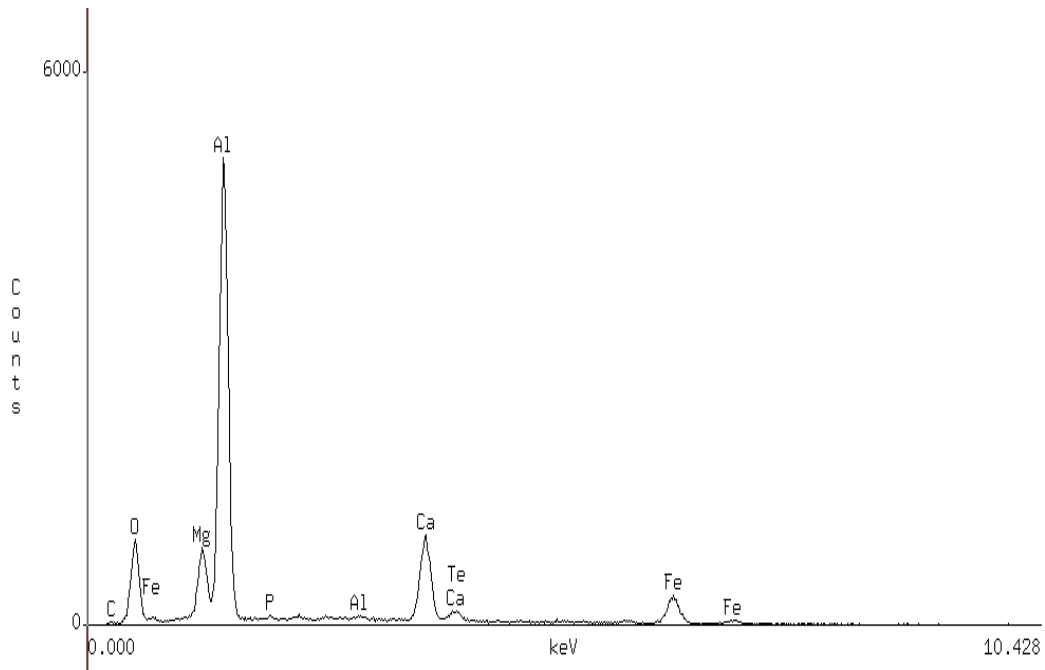


**Figure 2-8: A typical EDS spectrum highlighting which elements the NMI was made of. [2.1]**

## **2. Can Making defects (poor trim)**

Can defects which can affect flange integrity during can making include poor trimming. The drawn and wall ironed can is uneven around its top rim. The unevenness is trimmed off using rotary knives and sometimes the can may be cocked or angled on the trimmer spindle and a spiral trim result as indicated in the photograph below:

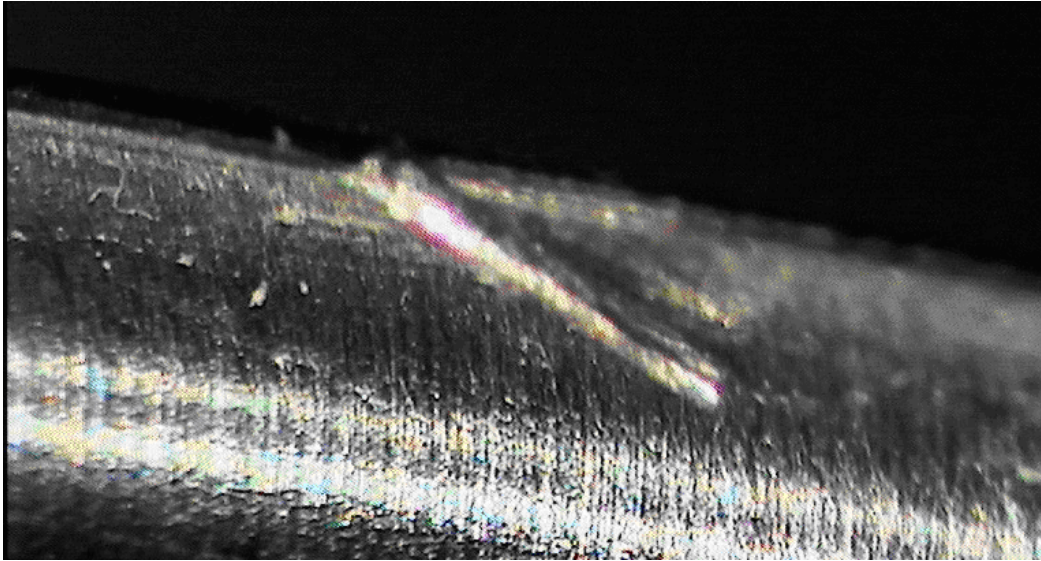


**Figure 2-9: A spiral trim. [2.1]**

Should the trim whisker break off, then a stepped can results. This is illustrated below:

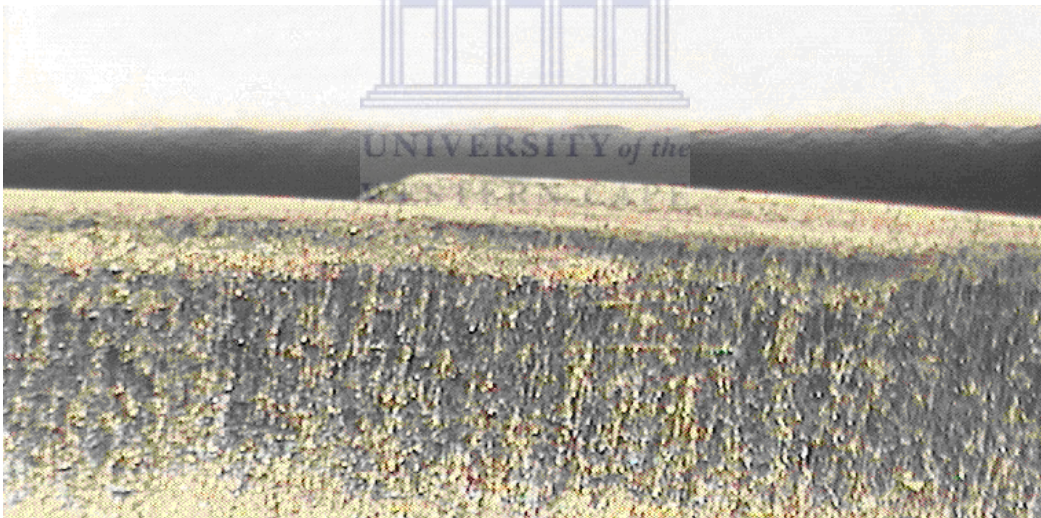


**Figure 2-10: A stepped can. [2.1]**

### 3) Can (Flange) Damage

This can occur anywhere in the supply chain. Such damage often results in a split flange \ body of the filled and processed can. An example of some damaged flanges is given in the following photographs:

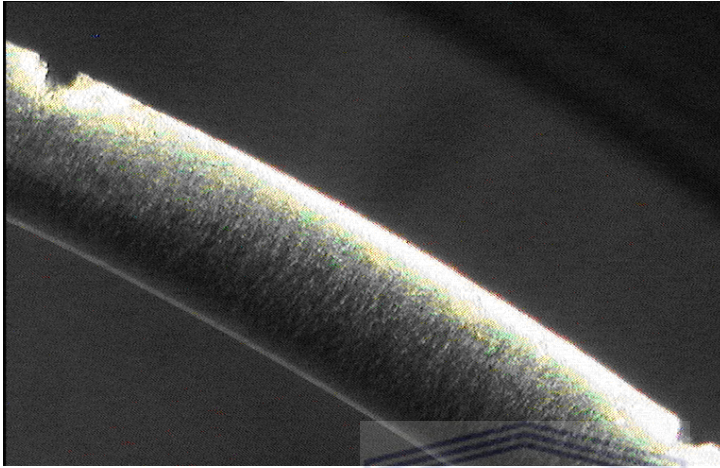


Figure 2-11: Damaged flange. [2.1]

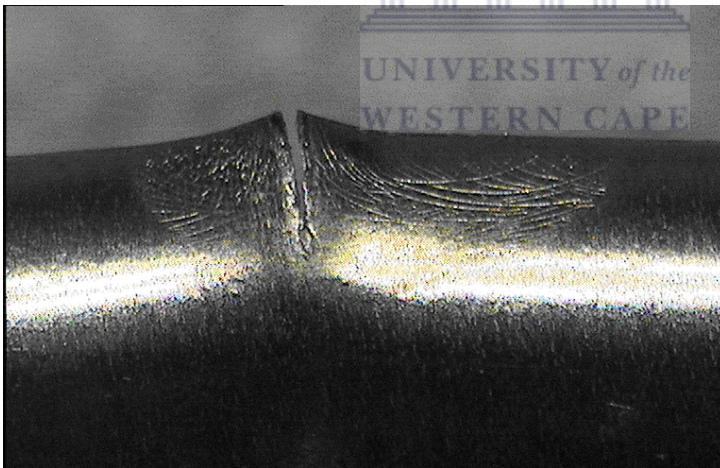
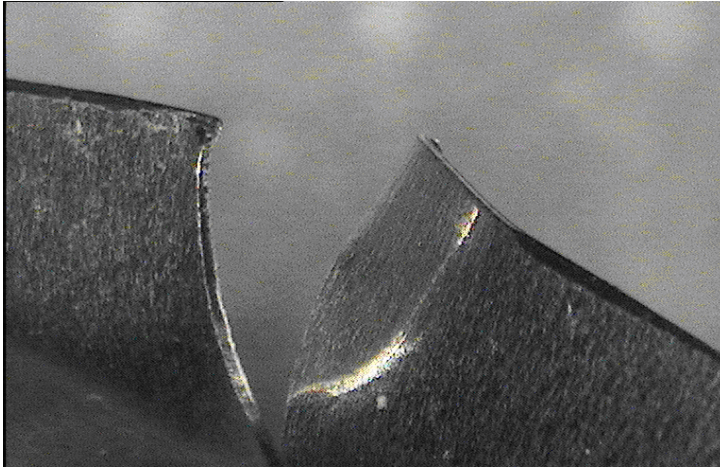


Figure 2-12: Damaged flange. [2.1]





**Figure 2-13: Damaged flange. [2.1]**

#### **4. Transport Damage (Peening)**

The fourth most common cause of split flanges is that caused during transportation of empty cans to the can filler. It is caused by high frequency vibration at very low loads of the flange of the can against the truck bulkheads or against steel top frames of the pallets. The term Peening was coined as the damage done to the edge of the flange by the high frequency / low load impacts is similar to that seen on the end of a cold chisel – the metal flows into a mushroom shape and this flow is accompanied by several very small fractures. Such fractures develop into split flanges / bodies on subsequent filling / seaming / processing.

Illustrations of this defect are given below:

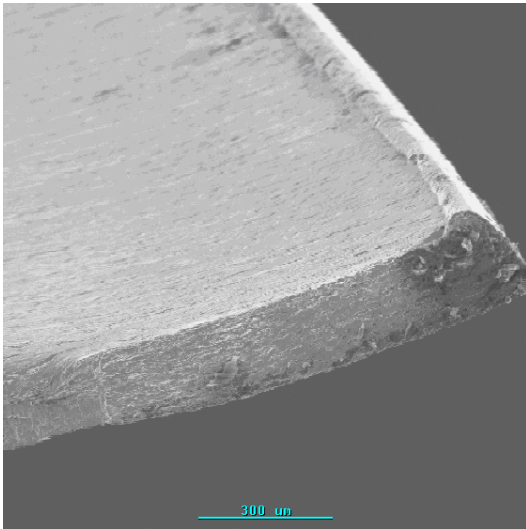


**Figure 2-14: Damage caused by peening. [2.1]**

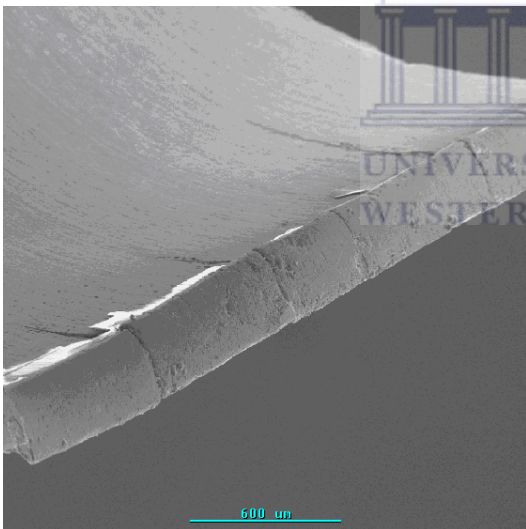


**Figure 2-15: damage caused by peening. [2.1]**

Sections of the split flange at the fracture face readily indicate the flow of metal into the characteristic “mushroom” shape.

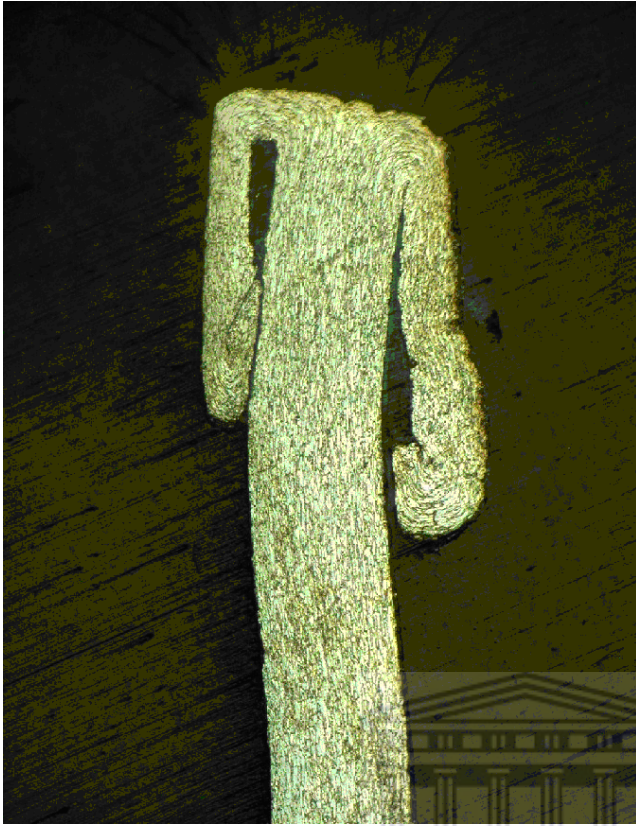


**Figure 2-16: The flow of metal into the characteristic mushroom shape. [2.1]**

UNIVERSITY of the  
WESTERN CAPE

## CHAPTER 3 ANALYTICAL TECHNIQUES

### 3.1 *Elastic Recoil Detection Analysis*

#### 3.11 Background

Elastic recoil detection (ERD) is an analytical technique giving information on the atomic composition profile of materials. For some years ion beam based analytical techniques have offered a wide range of possibilities like giving complementary information in the determination of the composition and structure of materials. Elastic Recoil Detection (ERD) is quite well accepted by the materials and solid state researchers' community because of its unique capabilities as a widely applicable analytical tool. The basic physical event in the technique is the elastic collision between the incoming and target nuclei [3.1].

In the analysis of solids, elastic recoil detection analysis (ERDA) generally allow the determination of the depth profiles, down to a depth resolution and absolute concentrations of monolayers of atoms in the surface layers of solids [3.2]. As the physical processes involved in this technique is very well understood, computer codes have been developed providing simple and efficient means of performing quantitative ERD analysis.

Hydrogen is a very important element that can modify mechanical, electrical, and optical properties of materials. The presence of hydrogen in a metal will most likely weaken its structure and cause cracking and failure of the material under stress or extreme environmental conditions. Hydrogen induced cracking (HIC) is a serious problem in oil pipes. Hydrogen atoms diffuse through a metal lattice because of their small size and form molecular hydrogen within the intermetallic vacancies of a metal. Molecules of hydrogen once formed within an internal structural defect remain trapped because of their larger size and generate a pressure that can be as high as 300 atmospheres which may cause severe damage [3.3]. This phenomenon is frequently referred as

hydrogen embrittlement [3.4]. There are several methods to detect hydrogen in a metallic structure. The commonly used methods of elemental analysis are not suitable or have limited applicability for the determination of concentration profile of hydrogen and most of the techniques are destructive. In contrast the Elastic Recoil Detection Analysis (ERDA) technique using 2-3 MeV  $\text{He}^{++}$  beams is a powerful non-destructive technique in profiling near surface hydrogen in non hydrogenous solids.

### **3.12) Theory**

#### **Basic Concepts**

Rutherford Backscattering (RBS) is based on collisions between atomic nuclei and derives its name from Lord Ernest Rutherford, who in 1911 was the first to prove experimentally the existence of positively charged nuclei in atoms. The measurement involves measuring the yield, and energy, of ions in a beam which backscatter after colliding with atoms in the near-surface region of a sample at which the beam has been targeted. With this information, it is possible to determine atomic mass and elemental concentrations versus depth below the surface. RBS is ideally suited for determining the concentration of trace elements heavier than the major constituents of the substrate. Its sensitivity for light masses, and for the makeup of samples well below the surface, is poor.

In RBS experiments, the detector is placed at an angle larger than  $90^\circ$  with respect to the beam direction and only backscattered projectiles are detected. The only parameter measured is the energy of the particles detected and based on that one determines the masses and depth distribution of the target constituents. In ERDA measurements, the detector is placed at angles smaller than  $90^\circ$  with respect to the beam direction. Target atoms that recoil out of the sample after scattering with  $\text{He}^{++}$  beam are detected. One of the main problems in ERDA is that these recoils need to be separated from the scattered projectiles. The measured energy distribution for the recoil is then used to determine its depth distribution in the sample, thus avoiding

ambiguity. The mass ratio between projectile and recoil mainly determines which technique can be used to perform that separation or identification. [3.5]

The energy measured for a particle backscattered at a given angle depends upon two processes. Particles lose energy while they pass through the sample, both before and after a collision. The amount of energy lost is dependent on the stopping power of the target material. The amount of energy lost in the projectile depends on the masses of the projectile and the target atoms. The ratio of the energies of the projectile before and after collision is called the Kinematic factor.

The number of backscattering events that occur from a given element in a sample depend upon two factors: the concentration of the element and the effective size of its nucleus. The probability that the beam and the material collide in such a way that the ejected hydrogen is directed towards the detector is called its scattering cross section.

### **Kinematic Factor: Qualitative Analysis**

For scattering at the sample surface the only energy loss mechanism is momentum transfer to the target atom. An important issue is that  $\text{He}^{++}$  will not scatter backwards from H atoms in a sample. Elements of comparable mass lighter than the projectile element will instead scatter in forward trajectories with significant energy. Thus, these elements cannot be detected using classical RBS. However, by placing a detector so that these forward scattering events can be recorded, these elements can be quantitatively measured using the same principles as RBS.

A classical geometry of a scattering experiment in the laboratory frame of reference is given in figure 3.1. A projectile of mass  $M_1$ , charge  $Z_1$  and with energy  $E_0$  impinges on a target atom at rest with mass  $M_2$  and charge  $Z_2$ . After collision, the projectile has energy  $E_1$  and is scattered at an angle  $\theta$  with respect to the direction of the incoming beam, while the target atom recoils at an angle  $\phi$  with energy  $E_2$ . The plane in which both particles move is defined as the scatter plane. The plane perpendicular to the scatter plane is defined

as the vertical plane. Restricting us to the case of elastic scattering, the energies of both the scattered projectile  $E_1$  (detected in RBS) and the recoil  $E_2$  (detected in ERDA) can be calculated from the laws of conservation of energy and momentum:

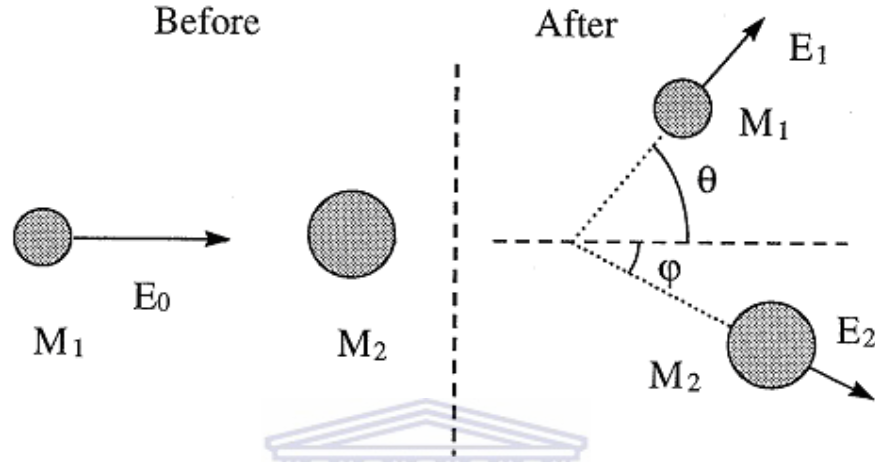


Figure 3-1: Schematic representation of a classical geometry of a scattering experiment in the laboratory frame of reference. Left is before and right is after the scattering event. [3.6]

$$E_1 = K_1 E_0 = \left[ \frac{M_1 \cos \theta \pm \left( M_2^2 - M_1^2 \sin^2 \theta \right)^{1/2}}{M_1 + M_2} \right]^2 E_0 \quad (3.1)$$

$$E_2 = K_2 E_0 = \frac{4M_1 M_2 \cos^2 \phi}{(M_1 + M_2)^2} E_0 \quad (3.2)$$

At a fixed angle of detection, the only factor affecting the kinematic factors,  $K_1$  and  $K_2$ , is the mass ratio,  $M_1/M_2$ . If  $M_1 < M_2$  then the plus sign in equation 3.1 holds and when  $M_1 > M_2$  there are two solutions resulting in possibly two kinematic factors. The kinematic factor  $K_1$  is for the scattered particle and  $K_2$  is the Kinematic Factor for the recoiled particle. The maximum angle at which projectiles can be scattered is  $\theta_{\max} = \arcsin(M_2/M_1)$ . It appears that the energy of the recoil particle is maximal when  $M_1 = M_2$ . Further, for  $M_2/M_1 > 1$  the kinematic factor for scattering of the primary particle is larger than the kinematic factor for recoiling and, importantly, increases with increasing the mass ratio. The consequence is that particles moving in the direction of a

detector, located at an angle smaller than  $90^\circ$  with the incident beam direction, have larger energies when they originate from a scattering process involving a heavy target: for  $M_2/M_1 < 1$  the largest energy is carried by the heaviest recoils and for  $M_2/M_1 > 1$  the scattered primaries have a larger energy when scattered at a heavier nucleus. The implication is that a simple measurement of the number and energy of particles at angles smaller than  $90^\circ$  do not result in an enhanced sensitivity for light elements when compared with RBS. [3.6]

### Scattering Cross Sections: Quantitative Analysis

The relative number of particles backscattered from a target atom into a given solid angle for a given number of incident particles is related to the differential scattering cross section. The scattering cross section is basically proportional to the square of the atomic number of the target atom. [3.7]

An important characteristic of each type of collision is the probability with which it takes place. The chance that one particle from the ion beam ejects a recoil ( $Z_2, M_2$ ) in such a way that it starts moving in the direction of the detector is proportional to the areal density (atoms.cm<sup>-2</sup>) of this element and the solid angle of the detector. The proportionality constant is known as the Rutherford differential cross section: [3.7]

$$\frac{d\sigma}{d\Omega} = \left( \frac{Z_1 Z_2 e^2}{2E_1} \right)^2 \frac{\left( 1 + \frac{M_1}{M_2} \right)^2}{\cos^3 \varphi} \quad (3.3)$$



$M_1$  and  $M_2$  are the masses of the projectile and the recoil respectively,  $\phi$  is the scattering angle and  $E_1$  is the energy of the recoiled atoms.

The total Yield  $Y_j$  of scattered projectiles or recoils for a specific element  $j$  as measured by the detector can be expressed as: [3.7]

$$Y_j = N_j Q \Omega \sigma_j \quad (3.4)$$

Where  $N_j$  is the number of target atoms per unit area,  $Q$  is the number of projectiles,  $\Omega$  is the solid angle of the detector and  $\sigma_j$  is the differential cross section averaged over the surface of the detector.

When the solid angle  $\Omega$ , the cross section  $\sigma_j$  and the number of incident projectiles  $Q$  are known, it is straight forward to calculate the areal density of the target atoms  $N_j$ , and straight forward to quantify the results. In practice  $\Omega$  and  $Q$  are difficult to determine accurately; standards are used to determine them accurately. In ERDA experiment a reference sample is used, i.e. a sample of well known composition. In this thesis, the areal densities are determined using Kapton reference ( $C_{22}N_2O_5H_{10}$ ) for which the composition is well known.

UNIVERSITY of the  
WESTERN CAPE

### **Stopping Power: Depth Profiling**

Ions propagating through matter lose kinetic energy in collisions with the target material. The so called stopping power is defined as the ion's energy loss per unit length:  $S = dE/dx$ . Sometimes the energy loss is expressed in terms of the so called stopping cross section  $\epsilon = 1/N (dE/dx)$ , where  $N$  is the particle density ( $10^{15}$  at/cm<sup>3</sup>) or  $\epsilon = 1/\rho (dE/dx)$ , where  $\rho$  is the mass density (g/cm<sup>3</sup>). When the stopping power is known, it can be used to extract depth information from measured energy spectra. This is illustrated in Figure 3.2 for an ERDA experiment at glancing angle geometry. A projectile impinges on the target at an angle  $\psi$ . A recoil originating from the surface has an energy  $E_2 = K_2 E_0$ . When the collision takes place at a depth  $t$ , the energy of the recoil upon leaving the sample at an angle  $\alpha$  is: [3.7]

$$E_3 = K_2 \left( E_0 - \frac{t}{\sin \psi} \int_{in} \frac{dE}{dx} dx \right) - \left( \frac{t}{\sin \alpha} \int_{out} \frac{dE}{dx} dx \right) \quad (3.5)$$

where the subscripts 'in' and 'out' denote the energy loss of the projectile on the inward path and the energy loss of the recoil on the outward path, respectively. The calculation of stopping powers is not straight forward, because they are a function of energy and sample composition. [3.7]

The energy difference  $\Delta E$  between recoil originating from the surface and recoil originating from depth  $t$  now becomes:

$$\Delta E = E_2 - E_3 = t \left( \frac{K_2}{\sin \psi} \int_{in} \frac{dE}{dx} dx + \frac{1}{\sin \alpha} \int_{out} \frac{dE}{dx} dx \right) \equiv t[S] \quad (3.6)$$

The symbol [S] is called the 'energy loss factor' and is the key to convert energy into depth information. It also relates the energy resolution  $\delta E$  to the depth resolution  $\delta t$  via  $\delta t = \delta E/[S]$ , where  $\delta t$  is the minimum thickness one can experimentally resolve.

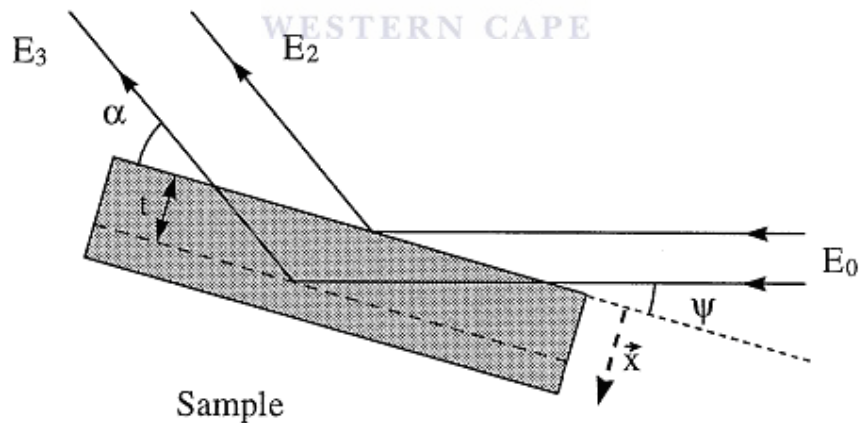


**Figure 3-2: Recoils scattered from the surface have energy  $E_2$ , while recoils scattered from depth  $t$  have energy  $E_3$ , the  $x$ -axis is perpendicular to the surface of the sample. [3.5]**

There are two main mechanisms responsible for energy loss. First, ions lose energy by collisions with the electrons of the target atoms (electronic stopping) and secondly, they lose energy in elastic collisions with the target nuclei as a whole ('nuclear' stopping). Projectile energies routinely used in

RBS or ERDA measurements, however, are in the order of 1 MeV or higher. Nuclear energy loss can then be neglected and inelastic collisions with the atomic electrons (electronic stopping) becomes the main interaction. [3.4]

Only a small fraction of the incident particles undergo a close encounter with an atomic nucleus and are backscattered out of the sample. The vast majority of the incident  $\text{He}^{++}$  atoms end up implanted in the sample. When the incoming beam penetrates to some depth in a dense medium, projectile energy dissipates due to interactions with electrons (electronic stopping) and to glancing collisions with the nuclei of target atoms (nuclear stopping). This means that a particle which backscatters from an element at some depth in a sample will have less energy than a particle which backscatters from the same element on the sample surface. The amount of energy a projectile loses per distance traversed in a sample depends on the projectile, its velocity, the elements in the sample, and the density of the sample material. Typical energy losses for 2 MeV He ranges between 100 and 800 eV/nm. This energy loss dependence on sample composition and density enables RBS measurements of layer thicknesses, a process called depth profiling.

The higher portion in energy loss is caused by electronic stopping which behaves (roughly) like friction between the probing particles and the electron clouds of the target atoms. Nuclear stopping is caused by the large number of glancing collisions which occur along the path of the probing atom. Nuclear stopping contributes significant energy losses only at low particle energies. The ratio of energy loss to two-dimensional atom density for a given material is known as its stopping cross section. Since the higher portion of energy loss is caused by interactions with electrons, the electronic structure of the target material has a significant affect upon its stopping power.

### Straggling and multiple Scattering: Limits in resolution

The loss of energy of an ion travelling is not a continuous process. It is rather a process where energy is lost in a large number of discrete steps, thus of statistical nature. When a beam of mono-energetic charged particles penetrates matter, statistical fluctuations in the exact number of interactions and in the energy transfer, result in a spreading of energy, a phenomenon called straggling. Since straggling broadens measured energy distributions, it puts a limit to depth and mass resolution. Bohr derived a simple expression for straggling in the high-energy limit [3.8]:

$$\Omega_B^2 = (1.44eVnm)^2 4\pi(Z_1)^2 NZ_2\Delta x \quad (3.7)$$

where  $\Omega_B$  is the Bohr value for the variance of the energy loss fluctuation  $\Omega$ ,  $\Delta x$  is the thickness of the traversed material and  $N$  is the atomic density of the target. Straggling increases with the square root of the path length in the material. At a certain depth in the sample, straggling will become larger than the other contributions to the inaccuracy of the energy measurement and will thus limit the energy resolution.

UNIVERSITY of the

Due to multiple small angle scattering events, the trajectories of incoming and outgoing particles in RBS and ERDA experiments are not completely straight. This effect is referred to as multiple scattering. Particles thus undergo deflections, which results in changes in angles  $\theta$  or  $\varphi$ . This influences both the Kinematic Factors and the cross sections.

### 3.13 Experimental Setup

The ERD measurements were made in the Van de Graaff accelerators facility at iThemba LABS in Cape Town. The 6.0 MV machine accelerated  $^4\text{He}$  ions as projectiles up to energies 3 MeV through a 2 mm collimator before they hit the sample kept in a chamber evacuated to vacuum pressures better than  $10^{-5}$  mbar. The sample was tilted to an angle of  $75^\circ$  with respect to the ion incident beam and a Surface Silicon Barrier (SSB) detector positioned at a recoil angle

of  $30^\circ$  was used to collect the recoiled atoms. The detector had an active area of  $100 \text{ mm}^2$ , a depletion depth of  $100 \mu\text{m}$  and a nominal resolution of  $15 \text{ keV}$ .

The implanted area was analysed by ERDA with a  $3\text{MeV He}^{++}$  beam at an incident angle of  $75^\circ$  with a scattering angle at  $30^\circ$ . The measured ERDA spectra have been converted into H depth profiles with a software package called SIMNRA. [3.9]

A  $\text{He}^{++}$  beam with energy of  $3 \text{ MeV}$  was used to analyse the H present in the timplate. A total charge of  $10000 \text{ nC}$  was collected each time with a current of  $40 \text{ nA}$ . SIMNRA 6, a simulation program for nuclear reactions was used to analyse the spectra.

Experimental Setup used in SIMNRA:

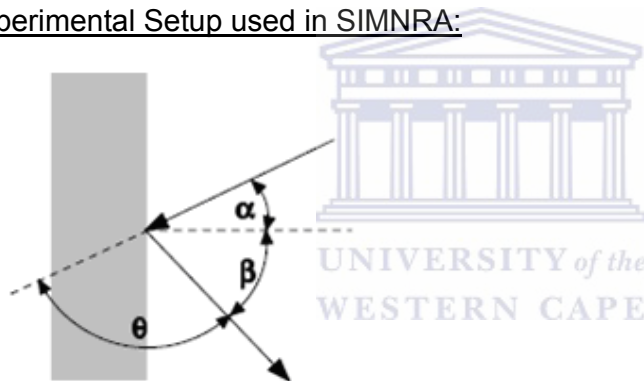


Figure 3-3: Geometry of a scattering experiment. Incident angle  $\alpha$ , exit angle  $\beta$  and scattering angle  $\theta$ . [3.8]

For ERDA:

$$\alpha = 75^\circ$$

$$\beta = 75^\circ$$

$$\theta = 30^\circ$$

### 3.14 Energy Calibration

A good energy per channel calibration was required for quantifying the results. This was done with three 125 $\mu\text{m}$  Kapton ( $\text{C}_{22}\text{H}_{10}\text{N}_2\text{O}_5$ ) reference standard samples. The first Kapton reference was bombarded with  $\text{He}^{++}$  particles at energy of 2.0 MeV and the current was set to 10 nA; the second Kapton reference was bombarded with  $\text{He}^{++}$  particles at energy of 2.5 MeV and the last one by 3.0 MeV. As these samples are calibrated reference standards, the signal was used for the determination of the product of the solid angle of the detector and dose, taking into account the depth of the implantation and screening effects for the evaluation of the scattering cross section. A Mylar foil with a thickness of 15  $\mu\text{m}$  was placed in front of the detector to prevent scattered  $\text{He}^{++}$  ions from being detected and to ensure that only H atoms are detected. The samples of interest were bombarded with  $\text{He}^{++}$  particles at 3.0MeV while the current was set to 40 nA.

A correlation between the recorded energies and channels was done using the following linear form:

$$E [\text{keV}] = A + B \times \text{channel} \quad (3.8)$$

where E is the particle energy, A the calibration offset and B the energy per channel factor. For illustration purposes fig.3.7 shows how the detected energies are related to the channels.

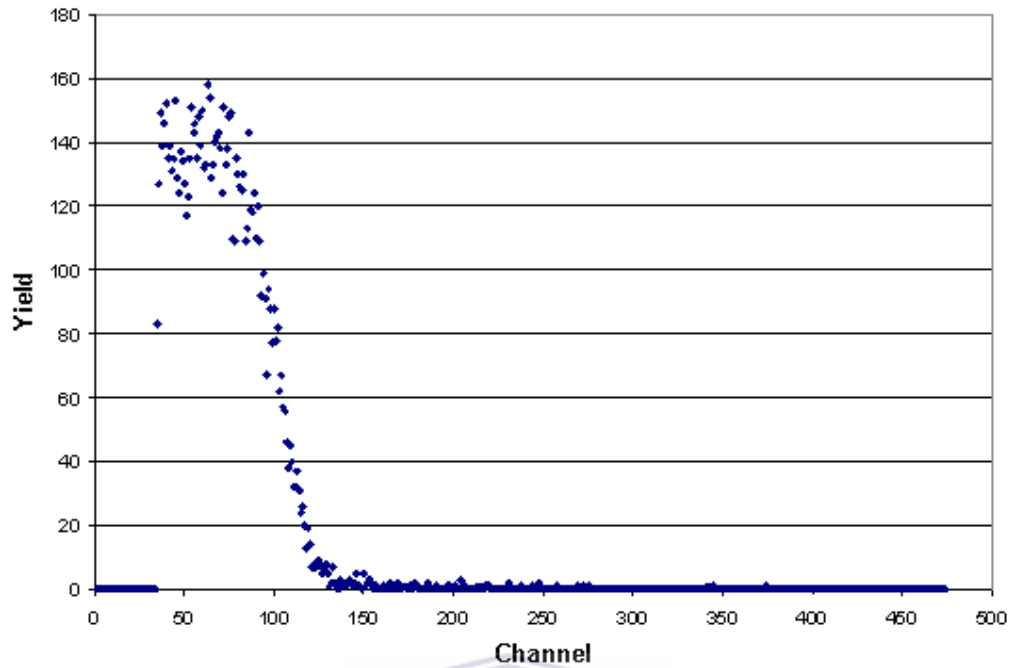


Figure 3-4: The spectrum from a kapton reference sample bombarded by 2 MeV  $\text{He}^{++}$  projectiles.

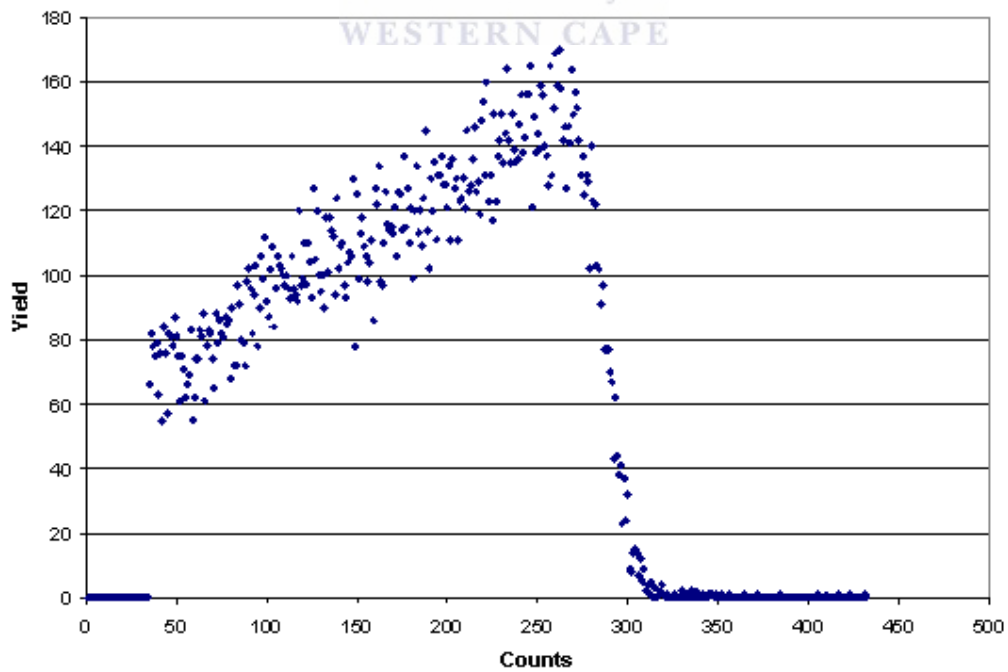


Figure 3-5: The spectrum from a kapton reference sample bombarded by 2.5 MeV  $\text{He}^{++}$  projectiles.

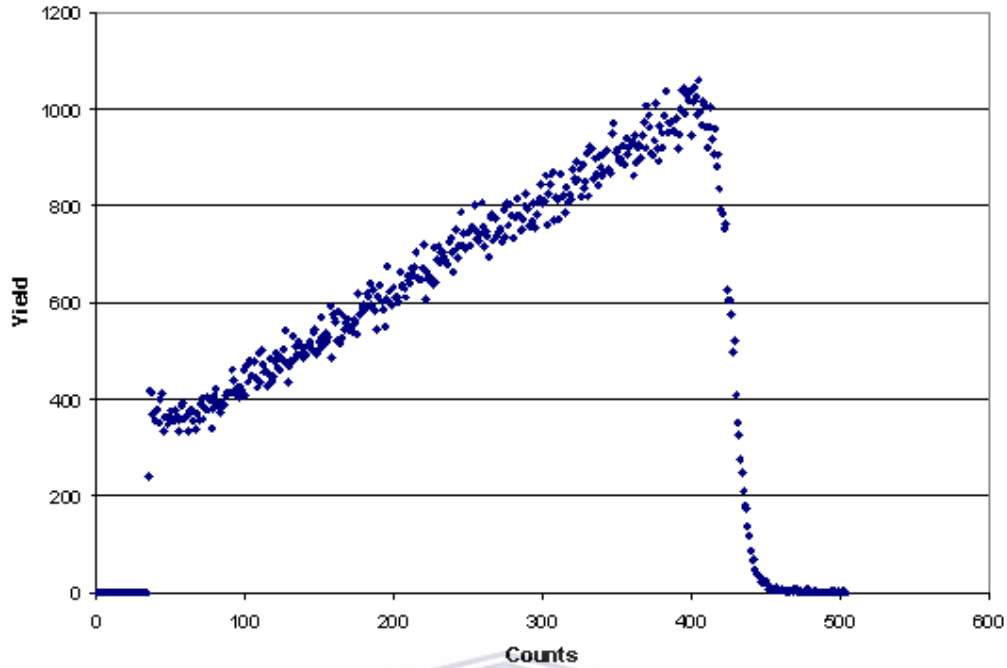


Figure 3-6: The spectrum from a kapton reference sample bombarded by 3 MeV He<sup>++</sup> projectiles.

Table 3-1: Data for energy calibration.

Channel Number	E <sub>0</sub> (keV)	E <sub>1</sub> (keV)	E <sub>loss</sub> (keV)	E <sub>detected</sub> (keV)
423	3000	1440	449.765	990.235
285	2500	1200	537.606	662.394
102	2000	960	719.988	240.012

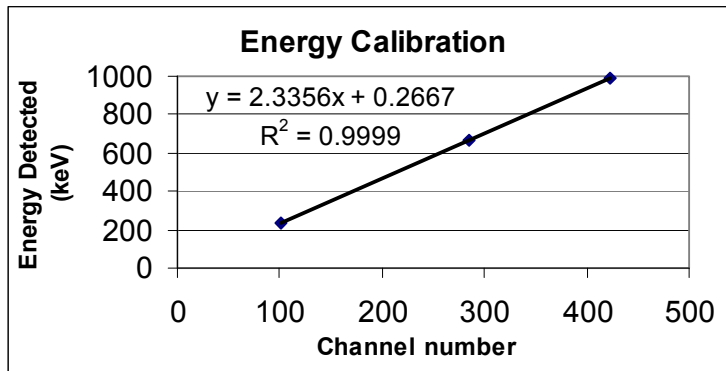


Figure 3-7: Energy-channel calibration experiment; the three points shown on the graph correspond to 3 calculated detected energies from an initial beam of 2, 2.5 and 3 MeV respectively.



In the above table the energy  $E_1$  was calculated from  $E_0$  based on the Kinematic factor between Hydrogen and Helium as discussed in section 3.22 and equation 3.2. The energy loss was calculated using an in build function in SIMNRA and takes into account factors like the scattering cross section and the stopping power of the target material as discussed in sections 3.23 and 3.24.

The energy calibration determined above is an initial estimate. The Kapton spectrum measured at 3 MeV was simulated to give the actual energy per channel ratio with the calibration offset.

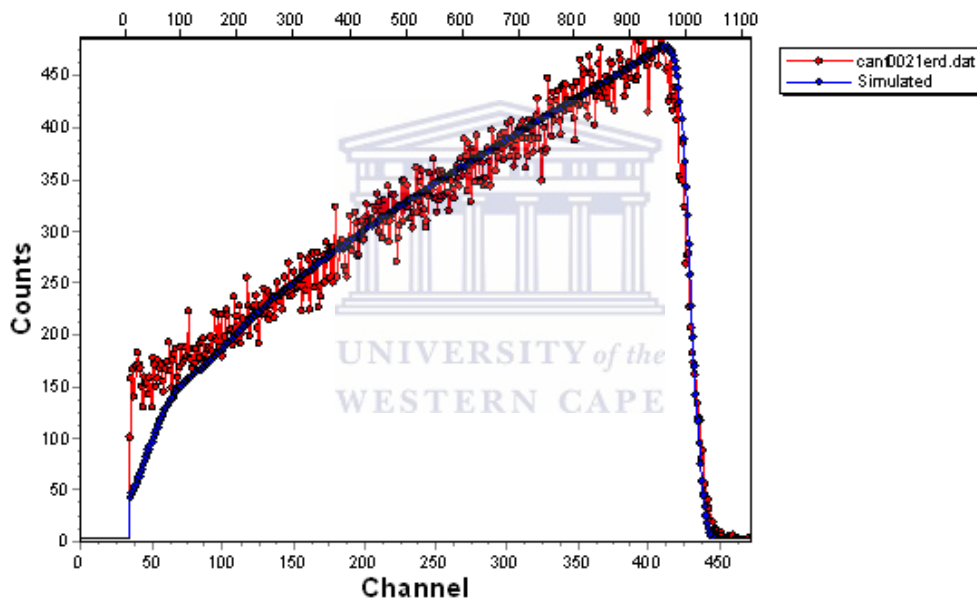


Figure 3-8: The simulated ERDA spectrum at 3 MeV.

**3.15 Thickness determinations of layers in monolayers****Table 3-2: Molar Mass details for Mylar foil**

<b>C<sub>10</sub>H<sub>8</sub>O<sub>4</sub></b>	<b>Element</b>	<b>Element Contribution</b>	<b>%</b>	<b>Atomic mass (g.mol<sup>-1</sup>)</b>	<b>individual contribution in mole (g.mol<sup>-1</sup>)</b>
	C	10	45.45	12.01	5.46
	H	8	36.36	1.008	0.37
	O	4	18.18	15.999	2.91
SUM	C <sub>10</sub> H <sub>8</sub> O <sub>4</sub>	22	100		8.73

The molar mass of the Mylar foil is 8.73g.mol<sup>-1</sup>, the density of the Mylar foil is 1.39g/cm<sup>3</sup> and Avogadro's constant is 6.02×10<sup>23</sup> atoms.mol<sup>-1</sup>.

$$\text{Atomic Density} = \frac{\text{Density} \times \text{Avogadro's Constant}}{\text{Molar Mass}}$$

$$\text{Atomic Density} = \frac{1.39\text{g.cm}^{-3} \times 6.02 \times 10^{23} \text{ atoms.mol}^{-1}}{8.73\text{g.mol}^{-1}} = 9.58 \times 10^{22} \text{ atoms.cm}^{-3}$$

$$\text{Areal Density} = \text{Atomic Density} \times \text{Thickness}$$

$$\text{Areal Density} = 9.58 \times 10^{22} \text{ atoms.cm}^{-3} \times 15 \mu\text{m}$$

$$\text{Areal Density} = 1.43701811 \times 10^{20} \text{ atoms.cm}^{-2}$$

$$\text{Areal Density} = 143701.81 \times 10^{15} \text{ atoms.cm}^{-2}$$

$$\text{Thickness} = 143701.81 \text{ monolayers}$$

**Table 3-3: Molar Mass details for Kapton standards**

<b>C<sub>22</sub>H<sub>10</sub>N<sub>2</sub>O<sub>5</sub></b>	<b>Element</b>	<b>Element Contribution</b>	<b>%</b>	<b>Atomic mass (g.mol<sup>-1</sup>)</b>	<b>individual contribution in mole (g.mol<sup>-1</sup>)</b>
	C	22	56.41	12.01	6.77
	H	10	25.64	1.008	0.26
	N	2	5.13	14.007	0.72
	O	5	12.82	15.999	2.05
SUM	C <sub>22</sub> H <sub>10</sub> N <sub>2</sub> O <sub>5</sub>	39	100		9.80

The molar mass of the Kapton is  $9.80\text{g}\cdot\text{mol}^{-1}$ , the density of the Kapton is  $1.42\text{g}/\text{cm}^3$  and Avogadro's constant is  $6.02\times 10^{23}\text{ atoms}\cdot\text{mol}^{-1}$ .

$$\text{Atomic Density} = \frac{\text{Density} \times \text{Avogadro's Constant}}{\text{Molar Mass}}$$

$$\text{Atomic Density} = \frac{1.42\text{g}\cdot\text{cm}^{-3} \times 6.02 \times 10^{23}\text{ atoms}\cdot\text{mol}^{-1}}{9.80\text{g}\cdot\text{mol}^{-1}} = 8.72 \times 10^{22}\text{ atoms}\cdot\text{cm}^{-3}$$

$$\text{Areal Density} = \text{Atomic Density} \times \text{Thickness}$$

$$\text{Areal Density} = 8.72 \times 10^{22}\text{ atoms}\cdot\text{cm}^{-3} \times 125\ \mu\text{m}$$

$$\text{Areal Density} = 1.090046271 \times 10^{21}\text{ atoms}\cdot\text{cm}^{-2}$$

$$\text{Areal Density} = 1090046.27 \times 10^{15}\text{ atoms}\cdot\text{cm}^{-2}$$

$$\text{Thickness} = 1090046.27\text{ monolayers}$$

### Can Layers

The thicknesses of the various layers in the samples used in the experiment were not known accurately, because the measurements of the different layers were done with the tinplate sheets by Nampak experts before the cans were made. The thickness of the layers after the cans were made will be calculated. The thickness of the Sn layer was  $0.354\ \mu\text{m}$  and the  $\text{FeSn}_2$  alloy was  $0.089\ \mu\text{m}$  before the metal plates are drawn into cans.

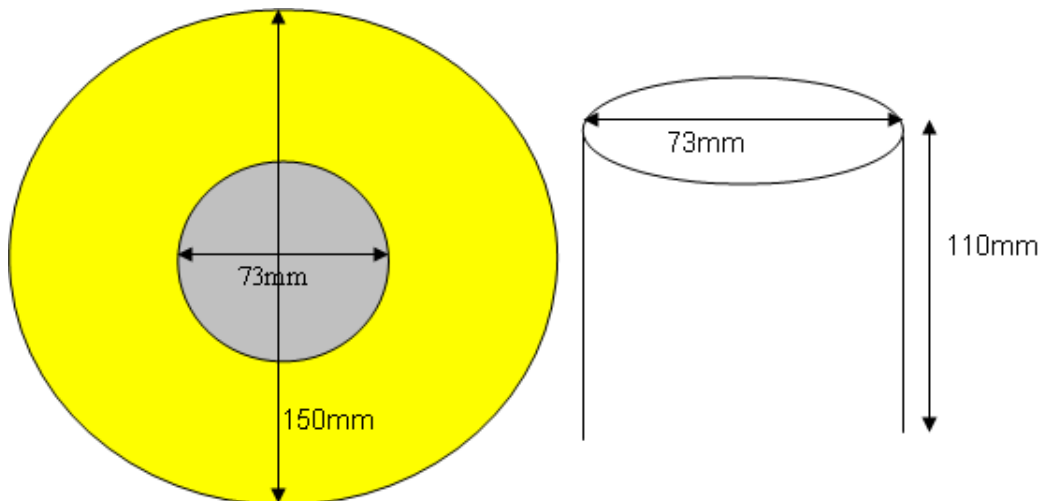


**Figure 3-9: The disc on the left is a tinplate sheet before it gets drawn into the can on the right.**

The inner disc is the base of the can which remains the same. It is the surface area coloured in yellow that forms the body of the can. So the ratio of the outer disc surface area and the surface area of the body of the can would determine by how much the tinsplate thickness was reduced and by how much the layer thicknesses was reduced. The thicknesses of the layers are reduced, because the surface area of the can is more than the surface area of the sheet.

Outer surface area of Disc:

$$A_1 = \pi(R^2 - r^2) = \pi(75^2 - 36.5^2) = 13486.072\text{mm}^2$$

Where R is the radius of the outer circle and r is the radius of the inner circle.

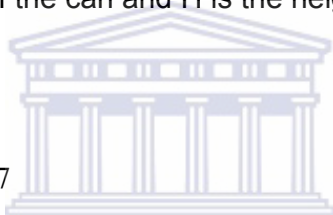
Surface Area of Can body:

$$A_2 = \pi DH = \pi \times 73\text{mm} \times 110\text{mm} = 25226.989\text{mm}^2$$

Where D is the diameter of the can and H is the height of the can.

Ratio:

$$\frac{A_2}{A_1} = \frac{25226.989\text{ mm}^2}{13486.072\text{ mm}^2} = 1.87$$



Based on the above Calculation each layer thickness is reduced by 1.87 times at the top of the can.

**Table 3-4: A comparison of the thicknesses before and after the can was drawn.**

Layer	Tinplate Sheet Thickness Before ( $\mu\text{m}$ )	Tinplate Can Thickness After ( $\mu\text{m}$ )
Sn	0.268	0.1433
FeSn <sub>2</sub>	0.089	0.0476

### Sn Layer

So the molar mass of the Sn is  $118.71\text{g}\cdot\text{mol}^{-1}$  and the density of the Sn is  $7.283\text{g}/\text{cm}^3$  [3.10] and Avogadro's constant is  $6.02 \times 10^{23}$  atoms. $\text{mol}^{-1}$ .

$$\text{Atomic Density} = \frac{\text{Density} \times \text{Avogadro's Constant}}{\text{Molar Mass}}$$

$$\text{Atomic Density} = \frac{7.283 \text{g.cm}^{-3} \times 6.02 \times 10^{23} \text{ atoms.mol}^{-1}}{118.71 \text{g.mol}^{-1}} = 3.69 \times 10^{22} \text{ atoms.cm}^{-3}$$

$$\text{Areal Density} = \text{Atomic Density} \times \text{Thickness}$$

$$\text{Areal Density} = 3.69 \times 10^{22} \text{ atoms.cm}^{-3} \times 0.1433 \mu\text{m}$$

$$\text{Areal Density} = 5.293131 \times 10^{17} \text{ atoms.cm}^{-2}$$

$$\text{Areal Density} = 529.31 \times 10^{15} \text{ atoms.cm}^{-2}$$

$$\text{Thickness} = 529.31 \text{ monolayers}$$

### FeSn<sub>2</sub> Layer

**Table 3-5: Molar Mass details for FeSn<sub>2</sub> layer in the can.**

FeSn <sub>2</sub>	Element	Element Contribution	%	Atomic mass (g.mol <sup>-1</sup> )	individual contribution in mole (g.mol <sup>-1</sup> )
	Fe	1	33.33	55.85	18.62
	Sn	2	66.67	118.71	79.14
SUM	FeSn <sub>2</sub>	3	100		97.76

$$\text{Density of FeSn}_2 = \frac{(\text{Fe} + 2\text{Sn})}{3} = \frac{7.867 + 2 \times 7.283}{3} = 7.478 \text{g.cm}^{-3}$$

So the molar mass of the FeSn<sub>2</sub> is 97.76g.mol<sup>-1</sup> and the density of the FeSn<sub>2</sub> is 7.478g/cm<sup>3</sup> and Avogadro's constant is 6.02×10<sup>23</sup> atoms.mol<sup>-1</sup>.

$$\text{Atomic Density} = \frac{\text{Density} \times \text{Avogadro's Constant}}{\text{Molar Mass}}$$

$$\text{Atomic Density} = \frac{7.478 \text{g.cm}^{-3} \times 6.02 \times 10^{23} \text{ atoms.mol}^{-1}}{97.76 \text{g.mol}^{-1}} = 4.605 \times 10^{22} \text{ atoms.cm}^{-3}$$

$$\text{Areal Density} = \text{Atomic Density} \times \text{Thickness}$$

$$\text{Areal Density} = 4.605 \times 10^{22} \text{ atoms.cm}^{-3} \times 0.0476 \mu\text{m}$$

$$\text{Areal Density} = 2.191616 \times 10^{17} \text{ atoms.cm}^{-2}$$

$$\text{Areal Density} = 219.16 \times 10^{15} \text{ atoms.cm}^{-2}$$

$$\text{Thickness} = 219.16 \text{ monolayers}$$

The above mentioned layers were necessary for inputs in SIMNRA. The software only recognizes thicknesses in monolayers.

After all the simulations are complete in SIMNRA, the hydrogen concentration at different depths in the sample is known. The average H concentration throughout the sample is calculated as follows:

$$\text{Average H conc} = \sum_1^n \frac{H_n t_n}{T} \quad [3.8b]$$

Where H is the H<sup>+</sup> concentration at a specific layer, t is the thickness at that specific layer and T is the total thickness and n is the number of layers in the sample.

## 3.2 Stress Analysis by XRD

### 3.2.1) FUNDAMENTAL CONCEPTS IN X-RAY DIFFRACTION

Diffraction methods of residual stress determination basically measure the angles at which the maximum diffracted intensity take place when a crystalline sample is subjected to x-rays. From these angles it is possible to obtain the interplanar spacing of the diffraction planes using Bragg's law. If the residual stress exists within the sample, then the d spacing will be different than that of an unstressed state. This difference is proportional to magnitude of the residual stress.

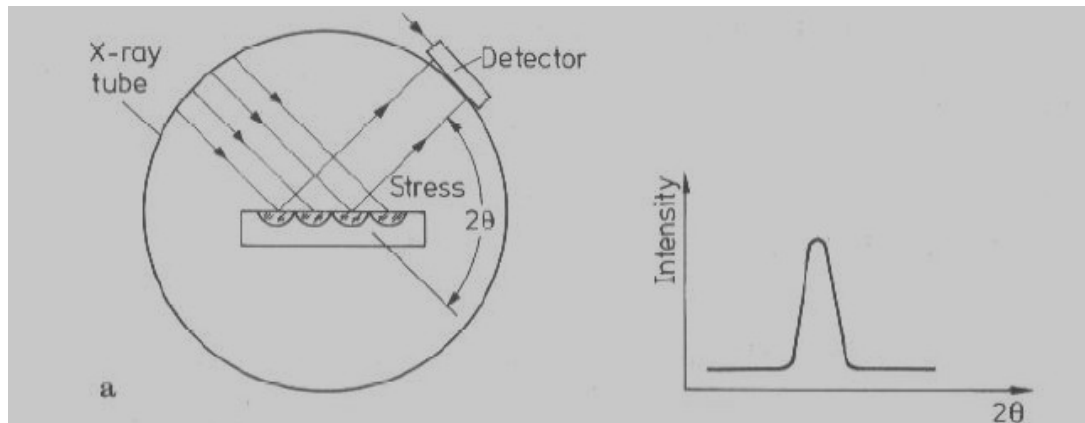
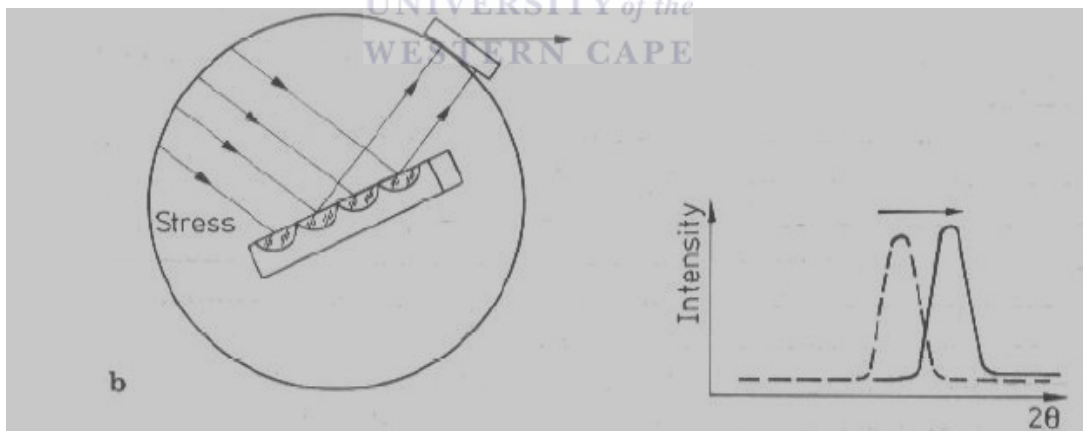


Figure 3-10: Diffractometer scheme. [3.10]

The incident beam diffracts X-rays of wavelength  $\lambda$  from planes which satisfy Bragg's law. If the surface is in compression then the planes are closer together than in the stress-free state because of Poisson's ratio. The interplanar spacing  $d$  is obtained from the peak in intensity versus scattering angle and Bragg's law [3.10].

With reference to Figure 3.10, assume that the detector is turned over a range of angles,  $2\theta$ , to find the angle,  $\theta$ , of the diffraction from grains which satisfy Bragg's law. In other words the grains that have planes of atoms with interplanar spacing "d" such that  $\lambda = 2d\sin\theta$ . The grains that have planes with this spacing that are parallel to the surface will diffract as in Figure 3.10. This diffraction occurs from a thin surface layer which is about 20  $\mu\text{m}$ . If the surface is in compression, then the interplanar spacing "d" is smaller than in the stress free state as a result of Poisson's effect. When the specimen is tilted with respect to the incoming beam new grains will diffract and the orientation of the diffraction planes is more nearly perpendicular to the stress direction (Figure 3.12).



**Figure 3-11: When the sample is tilted, diffraction will take place from other grains, but from the same planes (that satisfy Bragg's law). The peak takes place at higher values of  $2\theta$ . [3.10]**

As a result of the tilt, the  $d$  spacing decreases and the angle  $2\theta$  increases, as seen in the figures. In this case the  $d$  spacing acts as a strain gauge. Because of the fact that the interplanar spacing is so small, both micro and macro stresses will effect it. The XRD measures the sum of all these stresses.

### 3.2.2. X-ray Source

In early 1895, W. C. Roentgen (1845-1923) discovered that if the electrons are accelerated by a high voltage in a vacuum tube and allowed to strike a glass or metal surface, fluorescent minerals some distance away would glow, and photographic film would become exposed. He attributed these effects to a new type of radiation which are different from cathode rays. They were given the name X-rays which means an unknown quantity. X-rays are produced similar to Roentgen's today. X-rays are produced in a standard way: by accelerating electrons with a high voltage and allowing them to collide with a metal target. Electrons are produced by heating a cathode tungsten filament in a vacuum. The cathode is at a high negative potential, and the electrons are accelerated toward the anode, which is at ground potential. Then the electrons hit the anode with a very high velocity. The loss of energy results in x-rays. [3.11]

### 3.2.3. Absorption of X-rays

X-rays are attenuated when they pass through matter, thus the transmitted beam is weaker than the incident beam. Many different processes cause the decrease in the incident beam. Scattering (coherent & incoherent), heat production or excitations of photoelectrons, etc. are some of the contributors. The total loss in the intensity is termed absorption. The attenuation related to thickness of an infinitesimal slab is given by the relation [3.12]

$$\frac{dI}{I} = -\mu dz \quad (3.9)$$

where  $I$  is the intensity of the transmitted beam,  $\mu$  is the linear absorption coefficient. It is proportional to density and is usually listed as  $(\mu/\rho)$ . This ratio is known as mass absorption coefficient. It is a property of the material and independent of the material phase. Equation 3.9 can be integrated (for a homogenous finite slab thickness of  $z$ ) to give [3.12]

$$I_z = I_0 e^{(-\mu/\rho)\rho z} \quad (3.10)$$

where  $I_0$  is the intensity of the incident beam.



#### **3.2.4. Scattering of X-rays**

When a beam of x-rays is incident on the specimen, the photons collide with the electrons and scatter in different directions. There are two types of collisions. First type is elastic and the second one is inelastic. The former is the case when the x-rays collide with the electrons that are tightly bound to nucleus (usually the inner orbital electrons). There is no momentum transfer between the photon and electron which means scattered photon has the same energy and wavelength after the collision. This type of scattering is called coherent scattering. On the other hand, for the inelastic collision there is a momentum transfer from photon to electron. Due to this momentum transfer, photon loses energy and has longer wavelength. In the former there is a relation between phases of incident and scattered x-rays, whereas this is not the case for the latter. The latter is called Compton modified scattering or incoherent scattering. In both cases the photons are scattered in all directions.

#### **3.2.5. Bragg's Law**

When atoms spaced at regular intervals are irradiated by X-ray beams, the scattered radiation undergoes interference. Destructive interference occurs when the path difference is not a multiple of  $d$  and constructive interference is when the path difference is a multiple of  $d$ . The law that governs constructive interference (diffraction) is known as Bragg's law. When x-rays strike a crystal, the beam is reflected not only from the surface atoms but also from the atoms underneath the top surface to some considerable depth (Figure 3-12).

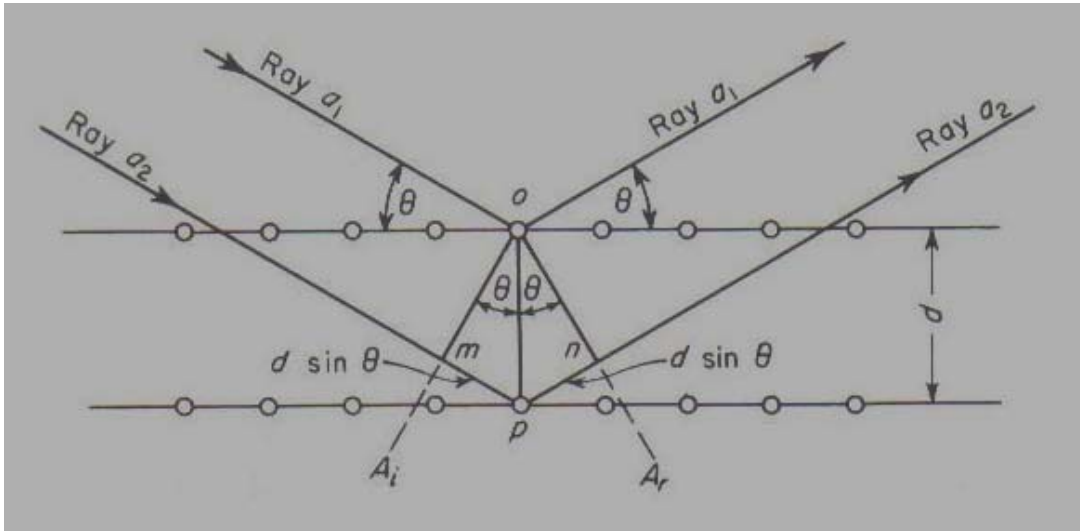


Figure 3-12: Diffraction of x-rays by a crystal and Bragg's law [3.11]

Figure 3-12 shows reflection of an x-ray beam from two parallel lattice planes. In reality there would be many other planes. In the figure, the distance between two parallel planes is represented by "d" (interplanar spacing). Lines  $A_i$  and  $A_r$  are drawn perpendicular to incident and reflected beams respectively. The line  $OA_i$  is a wave front. Point's o and m must be in phase because they lie on this line. The same condition is valid for point's o and n. This condition can be satisfied when the distance mpn equals a multiple of a complete wavelength. That is to say that it must equal  $n\lambda$  where n is an integer and  $\lambda$  is wavelength of x-rays. From the figure, the distances mp and np equal  $d\sin\theta$ . The distance mpn is  $2d\sin\theta$ . When this quantity equated to  $n\lambda$  we have: [3.11]

$$n\lambda = 2d\sin\theta \quad (3.11)$$

where  $n = 1, 2, 3, \dots$ ,  $\lambda$  is wavelength, d is interplanar spacing,  $\theta$  is angle of reflection.

This equation is known as Bragg's law.

### 3.2.6. Diffractometer Geometry

The diffractometer is the most common apparatus used for determining diffraction patterns. The diffractometer uses electronic counters, rotation tools to rotate the sample, and a detector to measure x-ray intensities. In Figure 3.9 the basic geometry of an x-ray diffractometer is shown. X-rays coming from an x-ray source strikes the specimen which is stabilized by a sample holder. The sample holder can be rotated around X axis perpendicular to the plane of the diffractometer. Then the diffracted beam is detected by a suitable detector. The detector can be rotated around X along the circumference of the diffractometer. The angle spanned by the detector can be limited to some degrees (in  $2\theta$  units). The step size and the time/step will depend on the accuracy you want to achieve and the statistics desired respectively.

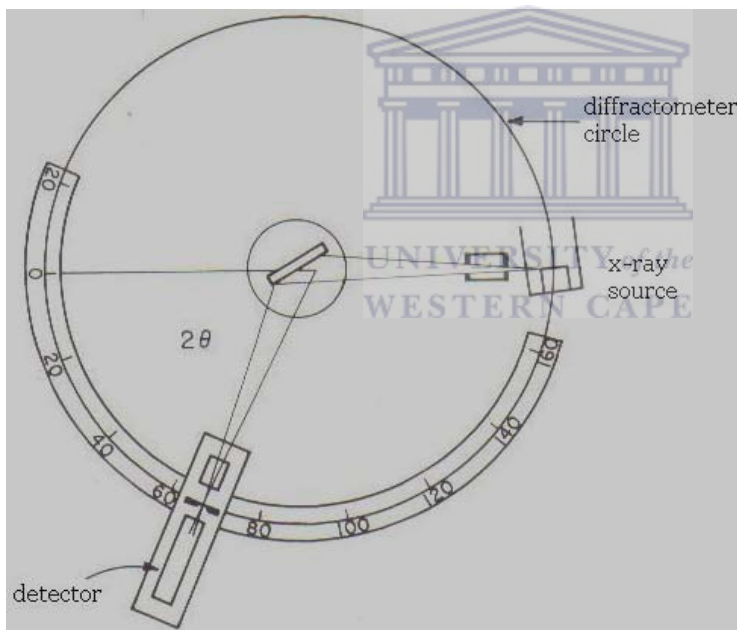
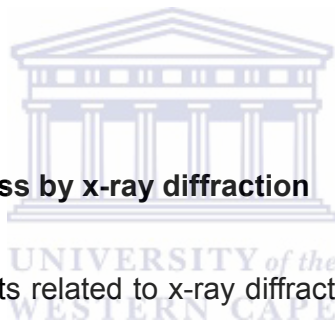


Figure 3-13: An x-ray diffractometer scheme [3.10].

The detector is moved along with the diffractometer circle to detect the diffracted beam.

### **3.2.7. Penetration Depth of X-rays**

The attenuation due to absorption limits the x-ray penetration depth. The penetration depth depends on the absorption coefficient of the material and the beam dimensions on specimen surface. Because attenuation of the incident beam is proportional to the thickness of the material it passes through, the contribution to the diffracted beam from layers deeper down in the material within the irradiated volume is less. Also because the diffracted beam has to traverse more material before leaving the surface, there will be more attenuation.



### **3.2.8. Calculation of stress by x-ray diffraction**

In this section the concepts related to x-ray diffraction and residual stress will be discussed. It is important to note that stress is not measured directly by the x-ray diffraction; it is always strain that is measured. Then the stress is calculated using appropriate equations of elasticity.

#### **3.2.8.1. Brief History on the Method**

This method was first proposed by Lester and Aborn in 1925. In 1930, Sachs and Weerts showed that the accuracy obtained was similar to other methods. In 1934 the method was improved by Barret and Gensamer which was used to measure sum of eigenstresses. In 1935, Glocker showed that it was possible to evaluate each of the eigenstresses. Since then, because of both technological improvements and better understanding of the deformation of the crystal lattice, especially the influence of anisotropy and crystallographic texture, remarkable progress was made on the method. Today, it is one of the most common techniques that is used to measure residual stress. [3.10]

### 3.2.8.2. Fundamental Equations

The orthogonal coordinate system in the following discussion is shown in Figure 3.14. There are two coordinate systems, the sample coordinate system  $S_i$  where  $S_1$  and  $S_2$  are on the surface. The second coordinate system is the laboratory coordinate system  $L_i$  and  $L_3$  is normal to the family of (hkl) planes whose spacing is measured by x-ray diffraction.  $L_2$  makes an angle  $\phi$  with  $S_2$  and is in the plane defined by  $S_1$  and  $S_2$ . In the following discussion primed tensor quantities refer to the Laboratory system  $L_i$  and unprimed tensor quantities refer to the sample coordinate system  $S_i$ . When the interplanar lattice spacing  $d$  is obtained from the diffraction peak for a given reflection hkl, the strain component along  $L_3$  can be obtained using the formula [3.10]:

$$\left(\varepsilon'_{33}\right)_{\phi\psi} = \frac{d_{\phi\psi} - d_0}{d_0} \quad (3.12)$$

where  $d_0$  is the unstressed interplanar spacing. The strain in equation 3.12 can be transformed to the sample coordinate system using tensor transformation.

$$\left(\varepsilon'_{33}\right)_{\phi\psi} = a_{3k} a_{31} \varepsilon_{k1} \quad (3.13)$$

where  $a_{3k}$ ,  $a_{31}$  are the direction cosines between  $L_3$ ,  $S_k$  and  $L_3$ ,  $S_1$

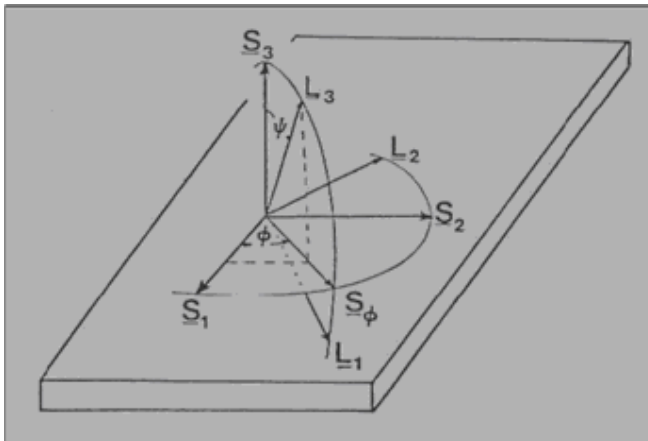


Figure 3-14: Sample and laboratory coordinate systems. [3.10]

$\omega$  is defined as a right-handed rotation about  $L_3$  axis. The  $\omega$  axis is fixed on the laboratory coordinates.

Then the direction cosine matrix will be: [3.10]

$$a_{ik} = \begin{vmatrix} \cos \phi \cos \psi & \sin \phi \cos \psi & -\sin \psi \\ -\sin \phi & \cos \phi & 0 \\ \cos \phi \sin \psi & \sin \phi \sin \psi & \cos \psi \end{vmatrix} \quad (3.14)$$

Substituting  $a_{3k}$ ,  $a_{31}$  in equation 3.13 one gets: [3.11]

$$\begin{aligned} \left( \varepsilon'_{33} \right)_{\phi\psi} = \frac{d_{\phi\psi} - d_0}{d_0} = & \varepsilon_{11} \cos^2 \phi \sin^2 \psi + \varepsilon_{12} \sin 2\phi \sin^2 \psi + \varepsilon_{22} \sin^2 \phi \sin^2 \psi \\ & + \varepsilon_{33} \cos^2 \psi + \varepsilon_{13} \cos \phi \sin 2\psi + \varepsilon_{23} \sin \phi \sin 2\psi \end{aligned} \quad (3.15)$$

Equation 3.15 is the fundamental relation that is used in x-ray diffraction for strain measurement.



### 3.2.8.3. Geometry Conventions in 2D-XRD systems

Figure 3.15 describes the geometric definition of diffraction cones in the laboratory coordinates system,  $X_L Y_L Z_L$ . Analogous to the conventional 3-circle and 4-circle goniometer, the direct X-ray beam propagates along the  $X_L$  axis,  $Z_L$  is up, and  $Y_L$  makes up a right-handed rectangular coordinate system. The axis  $X_L$  is also the rotation axis of the cones. The apex angles of the cones are determined by the  $2\theta$  values given by the Bragg equation. The  $\gamma$  angle is the azimuthal angle from the origin at the 6 o'clock direction ( $-Z_L$  direction) with a right-handed rotation axis along the opposite direction of the incident beam ( $-X_L$  direction). Since  $\chi$  has also been used to denote one of the goniometer angles in 4-circle convention,  $\gamma$  will be used hereafter to represent this angle. The  $\gamma$  angle here is used to define the direction of the diffracted beam on the cone. The  $\gamma$  angle actually defines a half plane with the  $X_L$  axis as the edge, referred to as  $\gamma$ -plane hereafter. Intersections of any diffraction cones with a  $\gamma$ -plane have the same  $\gamma$  value. The conventional diffractometer plane consists of two  $\gamma$ -planes with one  $\gamma = 90^\circ$  plane in the

negative  $Y_L$  side and  $\gamma = 270^\circ$  plane in the positive  $Y_L$  side.  $\gamma$  and  $2\theta$  angles forms a kind of spherical coordinate system which covers all the directions from the origin of the sample (goniometer center). The  $\gamma$ - $2\theta$  system is fixed in the laboratory systems  $X_L Y_L Z_L$ , which is independent of the sample orientation in the goniometer. This is a very important concept when we deal with the 2D diffraction data. [3.12]

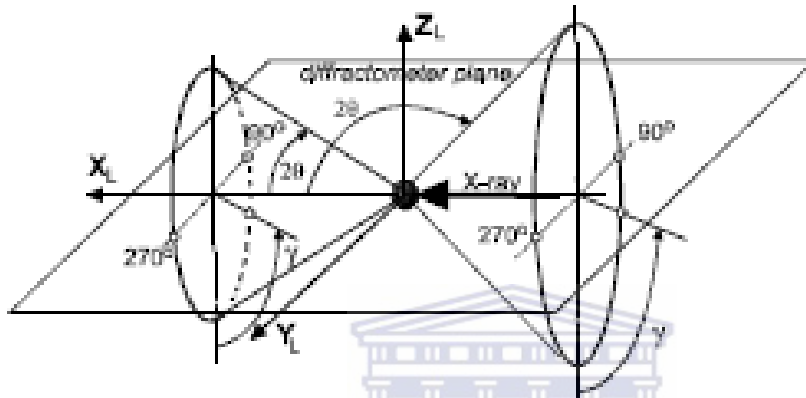


Figure 3-15: The geometric definition of diffraction rings in laboratory axes. [3.11]

#### 3.2.8.4. Stress Measurement with 2D-XRD

The two-dimensional (2D) diffraction pattern contains far more information than a one-dimensional (1D) profile collected with the conventional diffractometer. When used for stress measurement, 2D X-ray diffraction systems have many advantages over the conventional one dimensional diffraction systems in dealing with highly textured materials, large grain size, small sample area, weak diffraction, stress mapping, and stress tensor measurement. The stress measurement is based on the fundamental relationship between the stress tensor and the diffraction cone distortion. The benefit of the 2D method is that all the data points on diffraction rings are used to calculate stresses in order to get better measurement results with less data collection time.

The fundamental equation for strain measurement using a 2D detector is given by: [3.12]

$$f_{11}\varepsilon_{11} + f_{12}\varepsilon_{12} + f_{22}\varepsilon_{22} + f_{13}\varepsilon_{13} + f_{23}\varepsilon_{23} + f_{33}\varepsilon_{33} = \ln\left(\frac{\sin\theta_0}{\sin\theta}\right)$$

with:

Strain Coefficients	$F_{11}$	$f_{12}$	$f_{22}$	$f_{13}$	$f_{23}$	$f_{33}$
=	$A^2$	$2AB$	$B^2$	$2AC$	$2BC$	$C^2$

$a = \sin\theta \cos\omega + \sin\gamma \cos\theta \sin\omega$   
 $b = -\cos\gamma \cos\theta$   
 $c = \sin\theta \sin\omega - \sin\gamma \cos\theta \cos\omega$   
 $A = a \cos\phi - b \cos\psi \sin\phi + c \sin\psi \sin\phi$   
 $B = a \sin\phi + b \cos\psi \cos\phi - c \sin\psi \cos\phi$   
 $C = b \sin\psi + c \cos\psi$

UNIVERSITY of the  
WESTERN CAPE

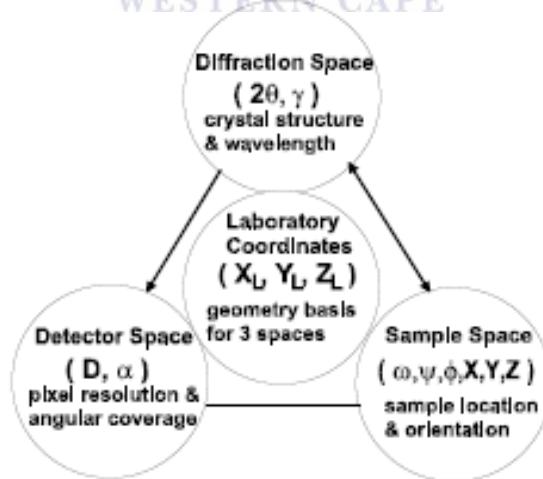


Figure 3-16: The relationship between the three spaces and the laboratory coordinates. [3.12]

### 3.2.8.5. True Stress Free Lattice D-spacing



In the Biaxial (2D) and Biaxial + Shear (2D) calculation, we have assumed that  $\sigma_{33}$  is zero so that we can calculate stress with an approximation of  $d_0$  (or  $2\theta_0$ ). Any error in  $d_0$  (or  $2\theta_0$ ) will contribute only to a pseudo-hydrostatic term  $\sigma_{ph}$ . Figure 3.17 shows the biaxial stress tensor measured from a shot peened Almen strip with different input  $d_0$  in the range of 1.165 Å to 1.175Å. The measured stress tensor is independent of the input  $d_0$ , ( $\sigma_{11}$  =623MPa,  $\sigma_{12}$  =638MPa,  $\sigma_{22}$  = 80MPa), where the pseudo-hydrostatic term  $\sigma_{ph}$  changes with the input  $d_0$ . The true  $d_0$  corresponds to the cross point of  $\sigma_{ph}$  line and zero stress.

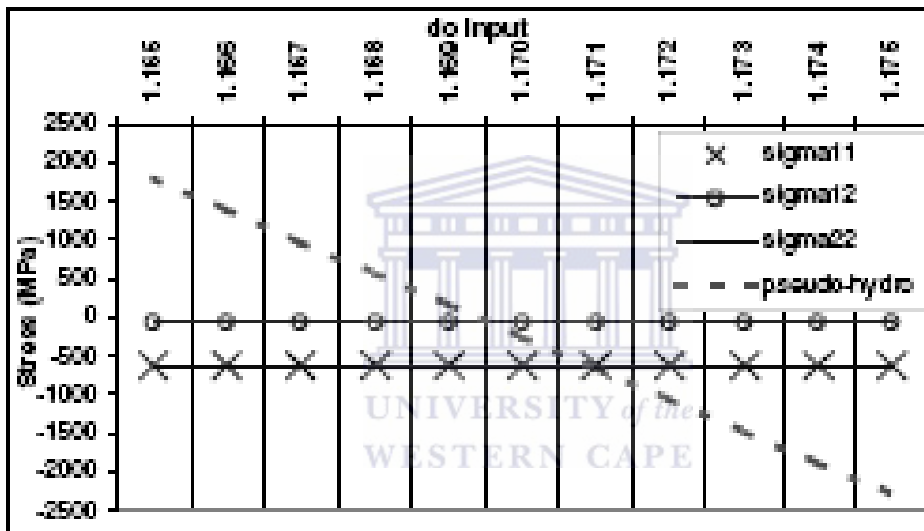


Figure 3-17: The measured biaxial stress tensor and pseudo hydrostatic stress as a function of input  $d_0$ . [3.11]

If we use  $d'_0$  to represent the initial input, the true  $d_0$  (or  $2\theta_0$ ) can be calculated from  $\sigma_{ph}$  with the following equations: [3.12]

$$d_0 = d'_0 \exp\left(\frac{1-2\nu}{E} \sigma_{ph}\right)$$

Or

$$\theta_0 = \arcsin\left[\sin \theta'_0 \exp\left(\frac{1-2\nu}{E} \sigma_{ph}\right)\right]$$

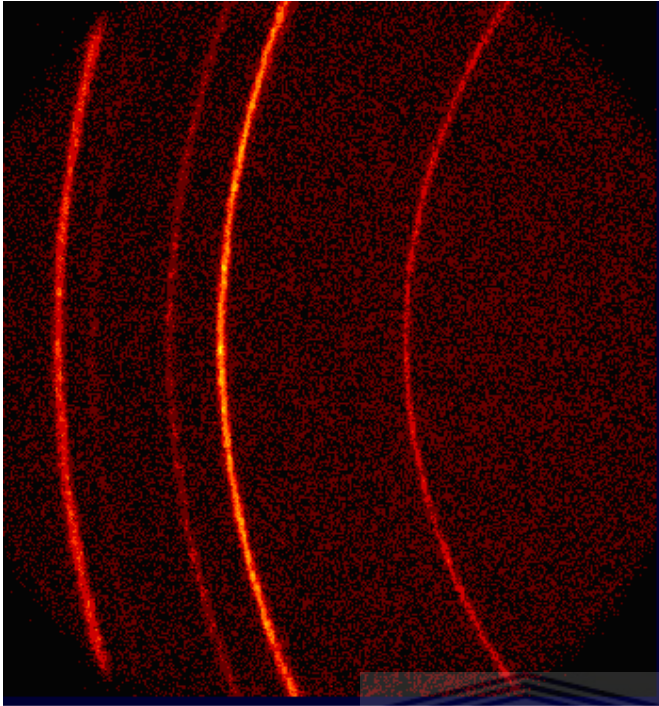


Figure 3-18: The diffracted rings detected by a 2D detector

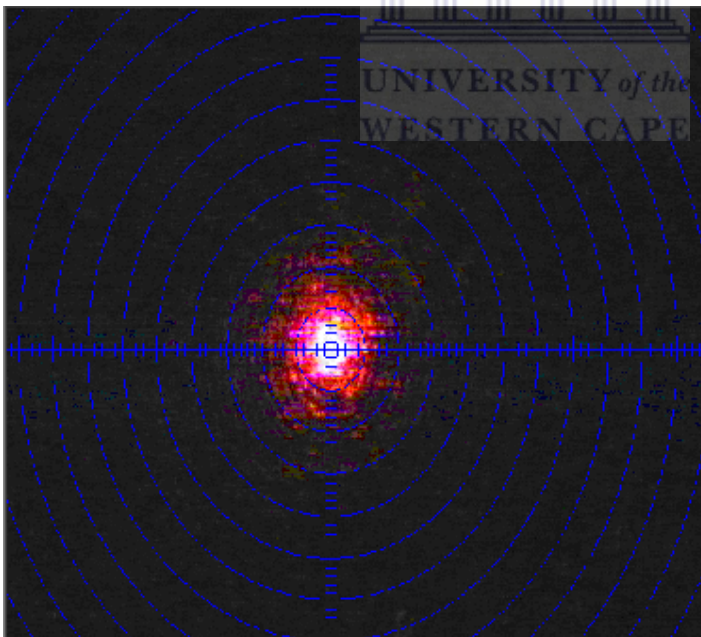


Figure 3-19: Red point focusing on the sample using the video alignment system

### **3.3 Tensile Testing**

#### **2.1-Young's Modulus**

In order to calculate Young's modulus for each material a graph of stress vs strain was needed, because the relation between stress and strain is: [3.11]

$$\sigma = E\varepsilon \quad (1)$$

where  $\sigma$  is the stress applied to the material, E is the Young's modulus and  $\varepsilon$  is the strain of the material. The stress is calculated from the force (F) applied to an area (A) of the material: [3.11]

$$\sigma = \frac{F}{A} \quad (2)$$

The strain of the material is expressed by the ratio between the extension and the original length of the material: [3.11]

$$\varepsilon = \frac{\Delta L}{L} \quad (3)$$

where L is the original length of the material and  $\Delta L$  is the extension.

#### **2.2-Tensile Strength**

When calculating the tensile strengths of the materials, a 2% offset line was drawn parallel to the elastic deformation straight line and the point where this line intersected the stress-strain graph was the margin between elastic and plastic deformation. So since the tensile strength of the material is the resistance of a material to permanently deform, this point where the 2% offset line intersects the graph is the strength of the material. A typical Stress vs Strain spectrum is shown below:

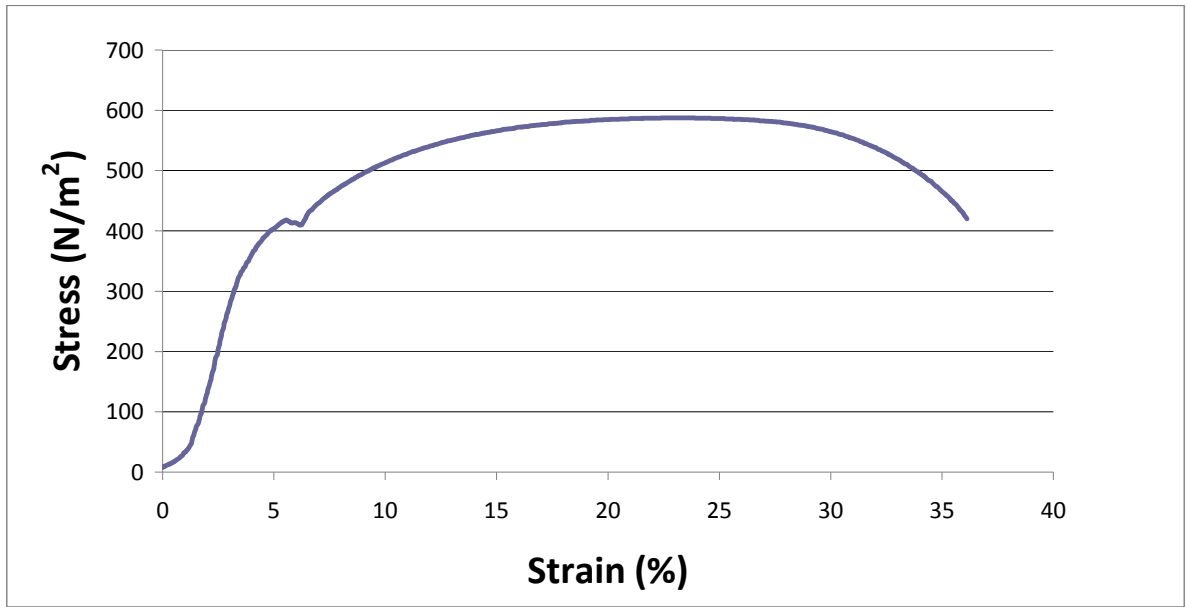


Figure 3-20: All the factors involved in a Stress Strain graph



## CHAPTER 4 EXPERIMENTAL PROCEDURE

### 4.1) Elastic Recoil Detection Analysis

Two sets of samples were prepared in this experiment. The first was to simulate an actual case of hydrogen embrittlement, using unprotected tinplate (i.e. no lacquer present). The second set of samples was used to investigate the hydrogen embrittlement in protected tinplate.

Firstly the top 2cm of all the cans were removed with a tin snips and guillotine. The sample was 2 cm wide and the length was the circumference of the can. These strips were cut into 1.5 cm length to fit the sample holder used for ERDA. The lacquer of the first set of samples were removed by dipping the samples for a few seconds stripping solution (900g Dimethylformamide, 50g oxalic acid and 50g water) heated to 98<sup>o</sup>C. The samples were prepared according to the table below:

Table 4-1: A comparison of the samples that will be prepared for ion beam analysis

No Steam	Steam
Untreated	Steam only
Acid	Acid
Fish + Tomato Sauce	Fish + Tomato Sauce

The steam was provided by a steam cooker that was heated by gas. All the steamed samples were exposed to steam for 33 min i.e. the time it took the cans to pass through the exhaust box at the canneries. The sample strips were placed on a metal plate full of holes in the steam cooker approximately 5 cm above the water to prevent the samples from being submerged in the water. This was to ensure that the samples were only exposed to steam. The clean samples had no other treatment apart from the steam, so the strip was placed directly onto the metal plate in the steam cooker. The samples exposed to acid were placed in a Petri dish filled with acid. The final samples were placed in a can filled with Fish. The samples that were not exposed to

steam were prepared in exactly the same way next to the steam cooker for exactly the same time periods and in the absence of any steam at normal room temperature under standard laboratory conditions. The samples were then dried with paper towel and placed into a Petri dish. These Petri dishes were placed in a dessicator to prevent any further air contamination.

## 4.2) Residual Stress Analysis by XRD

The sample preparation was relatively simple compared the other techniques used. The cans were sent through their respective treatments in the steam cookers then mounted onto the XRD machine. None of the cans were cut and none of the layers protecting the metal was removed.

The measurement was performed using a Bruker's D8 GADDS. Experimental setup on the primary side includes Co tube, graphite monochromator, 0.8mm collimator and a laser alignment system with an accuracy of 50 micron. The data were collected using a 2D detector. The analysis of data was done with a Bruker's Leptos v6 software. The measurement of strain was done in iso inclination geometry. The measurement details are given in table 7:

**Table 2: Measurement details from the Brukers Leptos v6 software:**

Omega range:	75 deg to 135 deg
Omega step size:	10 deg
Psi:	0 deg
Measurement time :	150s
<b>Generator settings</b>	
Voltage:	35 kV
Current :	35 mA

Due to the hardware limits of the diffractometer, the 310 peaks for Co could not be detected. The Co radiation peak is at  $161^{\circ}$  compared and the Cu radiation peak is at  $116^{\circ}$ . The peak 220 peak for cobalt was used at  $123^{\circ}$ . The peaks referred to above are from the hkl planes that are diffracting the x-rays to form constructive interference.

### **4.3) Tensile Testing**

The cans went through their respective treatment in the steam cooker. The split flanges occurred at the top 2cm of the cans. The top 2cm of the cans were removed and further trimmed to 1.8 cm in width using a guillotine. The samples were cut into 22 cm lengths which conformed to ASTM standards.

The mid section of the samples was machined to form the standard dumbbell shape of a typical tensile. The new width of the mid section of the sample was measured with a micrometer. Before the thickness of the steel could be measured, all the protective layers had to be removed in the middle of the sample. The lacquer stripping solution was used to remove the lacquer and a detinning solution was used to remove the tin. The thickness of each sample was then measured using a digital micrometer. Once the preparation of the samples finished, the computer system and the tensile tester was calibrated. The samples were then firmly mounted to the tensile tester and stretched till the sample was fractured. The results were displayed digitally.

## CHAPTER 5 RESULTS AND DISCUSSION

### 5.1) Elastic Recoil Detection Analysis

For ERDA two sets of results will be presented. The first set of samples was sent through the steam process without protection (no lacquer). This was done to check if the metal was susceptible to H embrittlement in the exhaust box without protection. It was also done to check if ERDA was a suitable technique for checking if H embrittlement could be caused by steam in an exhaust box. The second set of samples had protection. All the experimental data was simulated in SIMNRA in order to probe into the H-depth profile. A few of the simulated spectra are shown below; the scattered data are the experimental while the yellow continuous curve is the simulated spectrum.

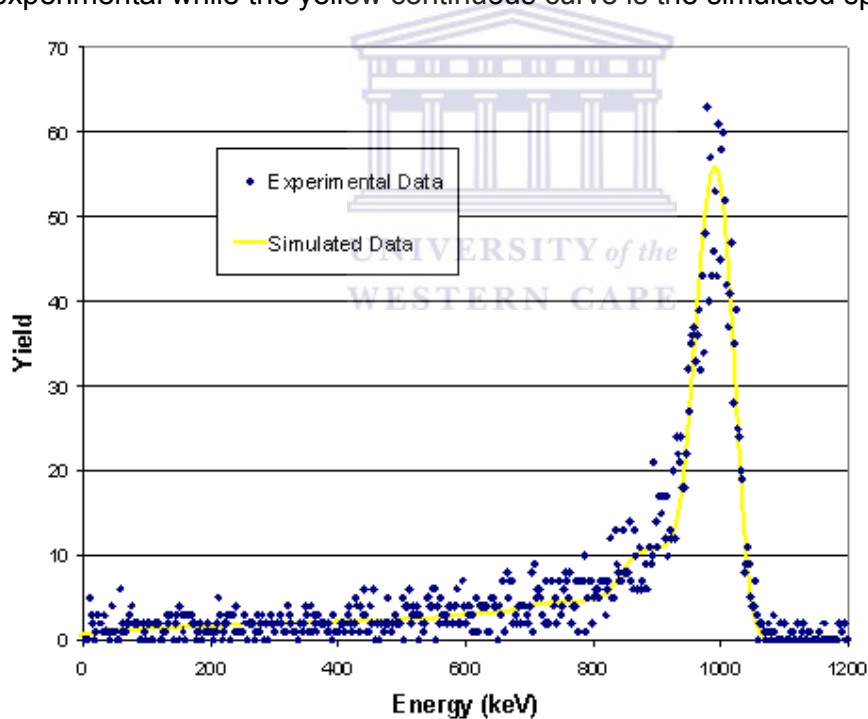


Figure 5-1: A simulated ERDA spectrum for a sample with no H treatment.



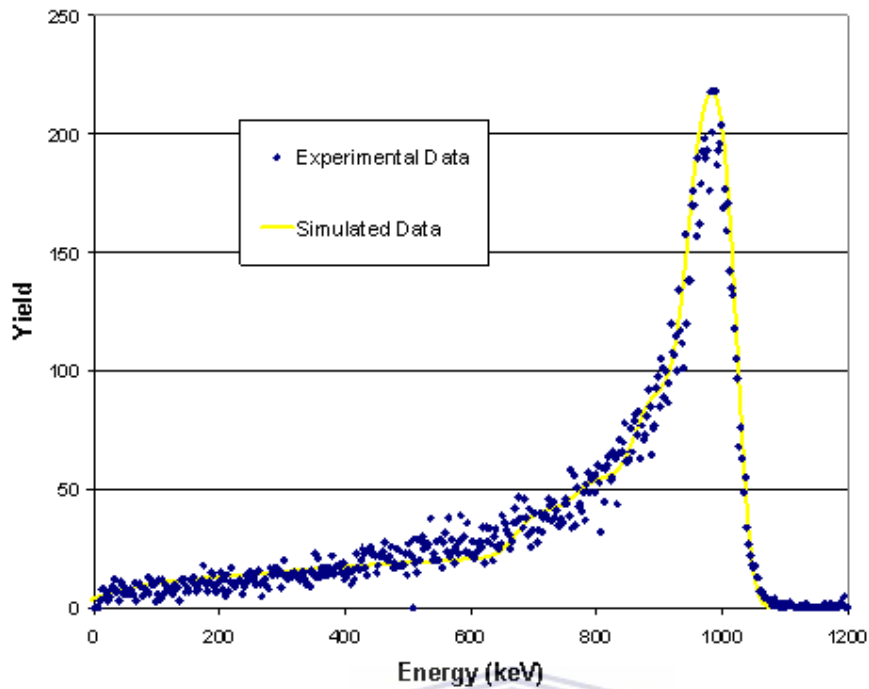


Figure 5-2: A simulated ERDA spectrum for the sample exposed to steam only.

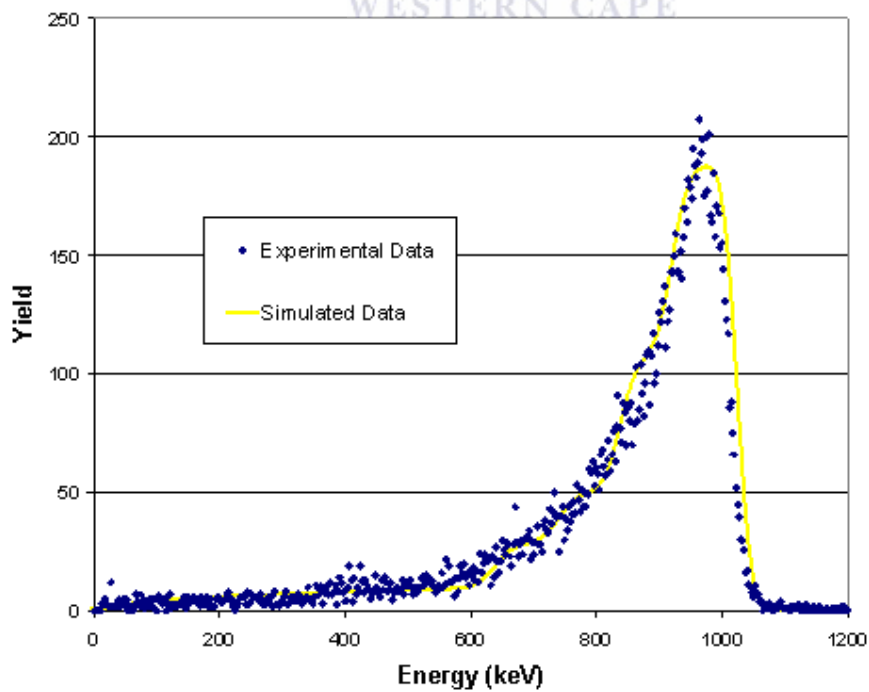
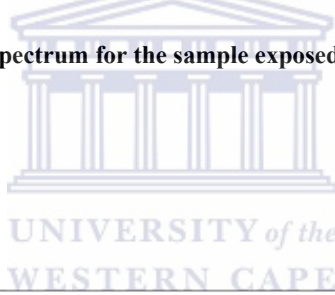


Figure 5-3: A simulated ERDA spectrum for the sample exposed to steam and acid

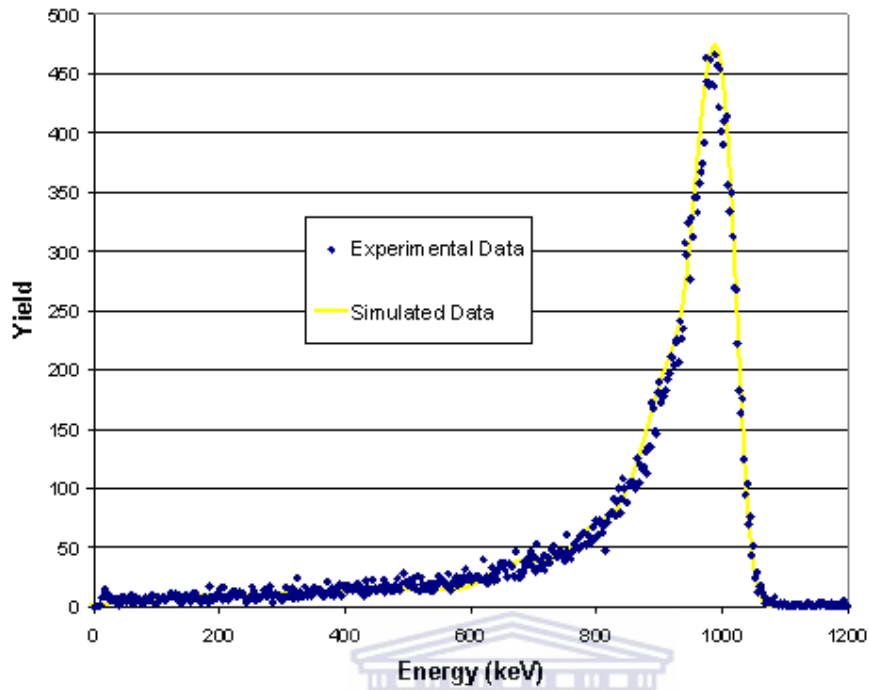


Figure 5-4: A simulated ERDA spectrum for the sample exposed to steam and fish.

After the experimental data were simulated, they were checked for consistency. This was done by preparing each sample type twice and checking if the spectra were repeatable. Two of the comparisons are shown below:

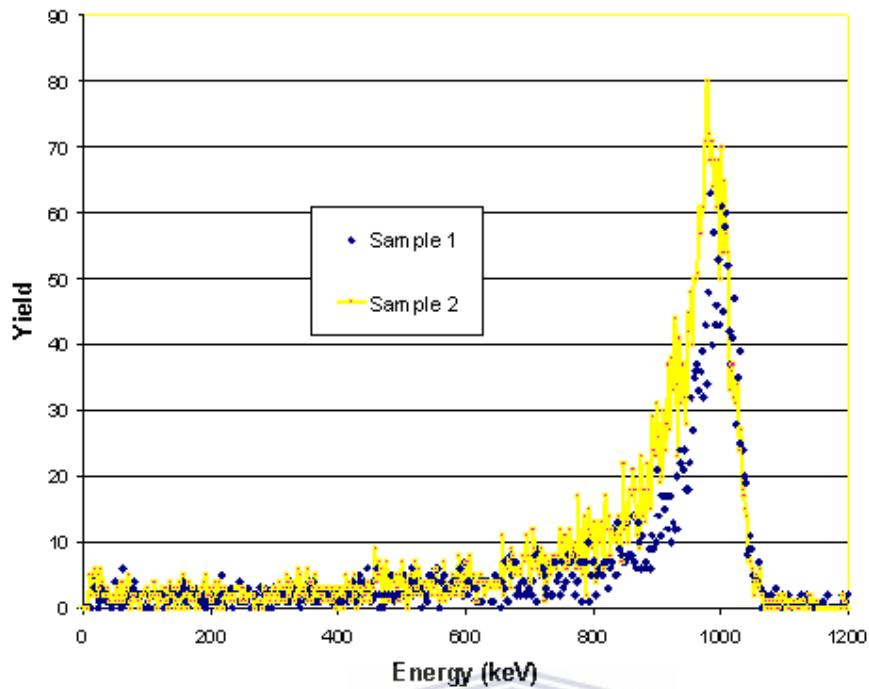


Figure 5-5: A comparison of two ERDA spectra for different samples with no H treatment.

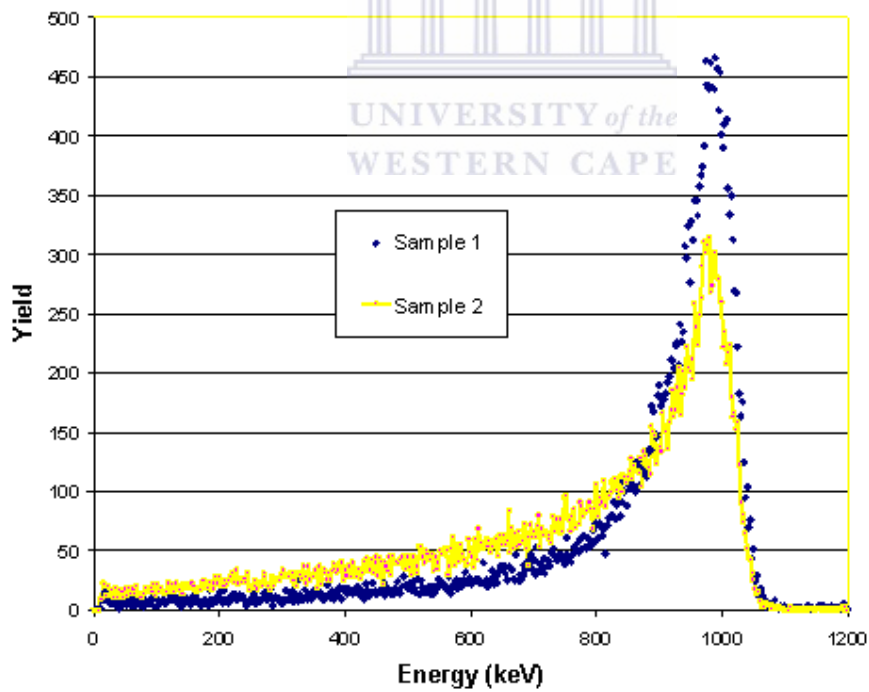
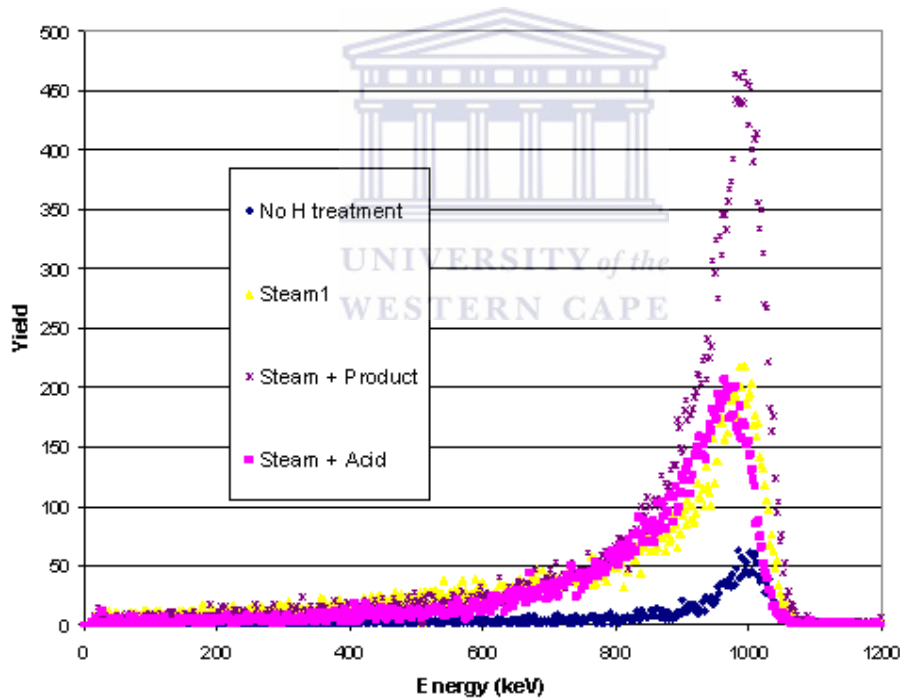


Figure 5-6: A comparison of two ERDA spectra for different samples treated with steam and product.

## Results and Discussion

Every sample prepared had a duplicate and both were measured to check for consistency. All of the samples that were prepared similarly had similar spectra and fitted on each other like the two spectra for the samples exposed to steam in fig 5.5. All the spectra had the same profile but the yields were different at the surface level only. The 1<sup>st</sup> sample had more surface hydrogen but less hydrogen deeper in the metal compared to the second sample. The 1<sup>st</sup> measurement could have been taken at one of the voids in the sample where more hydrogen collected closer to the surface.

The above spectra showed the samples were prepared consistently. The next step was to compare the samples prepared with different conditions. The following figure will show how different the spectra looks compared to the sample parameters.



**Figure 5-7: A comparison of the ERDA spectra for differently prepared samples with no protection.**

The above spectra show the exact same trend for all the samples regardless of how they were prepared. Based on this fact, all the samples should have higher hydrogen concentrations at the surface levels as compared to levels

deeper in the sample. The samples exposed to steam only and the samples exposed to steam and acid fits has comparable spectra. This means that the concentration of hydrogen of these samples would be similar. It is observed that the hydrogen content in these samples is higher than that in samples prepared with no hydrogen treatment. The samples that were exposed to steam and fish had the most surface hydrogen and the most hydrogen that diffused deeper into the material as well.

Based on the above discussion ERDA was a useful technique to determine whether or not hydrogen diffused into the metal. It appears that when unprotected tinplate was exposed to steam a definite hydrogen uptake occurred in the samples. And when unprotected tinplate was exposed to steam and fish even higher hydrogen uptake occurred in the samples.

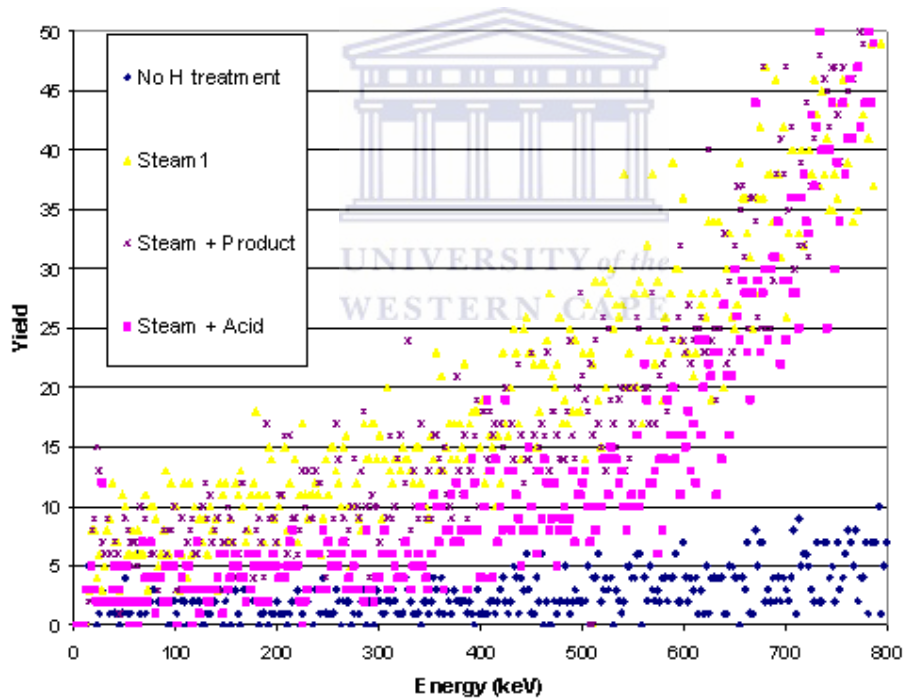


Figure 5-8: A close up on the ERDA spectrum for differently prepared samples with different treatment.

By taking a closer look at the spectrum the samples with no treatment, the yield moves closer down to background much quicker than any of the samples. As expected less hydrogen penetrated far deeper in samples with

## Results and Discussion

no hydrogen treatment. The samples exposed to steam and acid had less hydrogen penetrating deeper into the metal compared to the samples exposed to steam only and steam and product. The samples exposed to steam only had a similar amount of hydrogen penetrating into the metal compared to the samples exposed to steam and fish. This above discussion was summarized into a depth profiling figure below.

The information obtained from the spectra displayed in figure 5.9 was the depth profiling of the samples and the exact H concentration in the sample. The depth profiling of all the differently prepared samples are shown below:

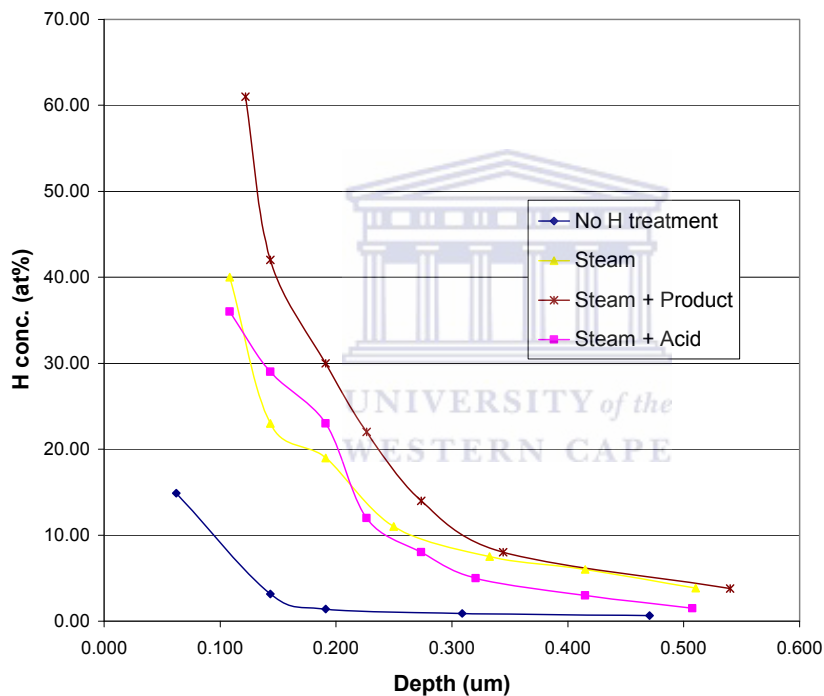


**Figure 5-9: A depth profiling curve for differently prepared samples with no lacquer protection.**

A depth profiling curve was compiled by layers of various thicknesses in the tinplate sample.

**Table 3: A sample with no treatment with different layers with their thicknesses**

		<b>Layer Thickness</b> <b>(1015Atoms/cm2)</b>	<b>Film Thickness</b> <b>(µm)</b>	<b>Film Thickness</b> <b>(µm)</b>	<b>H concentration</b> <b>at %</b>
<b>Layer</b>	<b>1</b>	230.00	0.062	0.062	14.88
<b>Layer</b>	<b>2</b>	299.31	0.081	0.143	3.16
<b>Layer</b>	<b>3</b>	219.16	0.048	0.191	1.40
<b>Layer</b>	<b>4</b>	1000.00	0.118	0.309	0.90
<b>Layer</b>	<b>5</b>	1370.55	0.162	0.470	0.64

When the H<sup>+</sup> concentration in the steel matrix was calculated, both surface layers were excluded. The average H concentrations throughout the sample and the average H concentration in the Steel matrix are shown below:

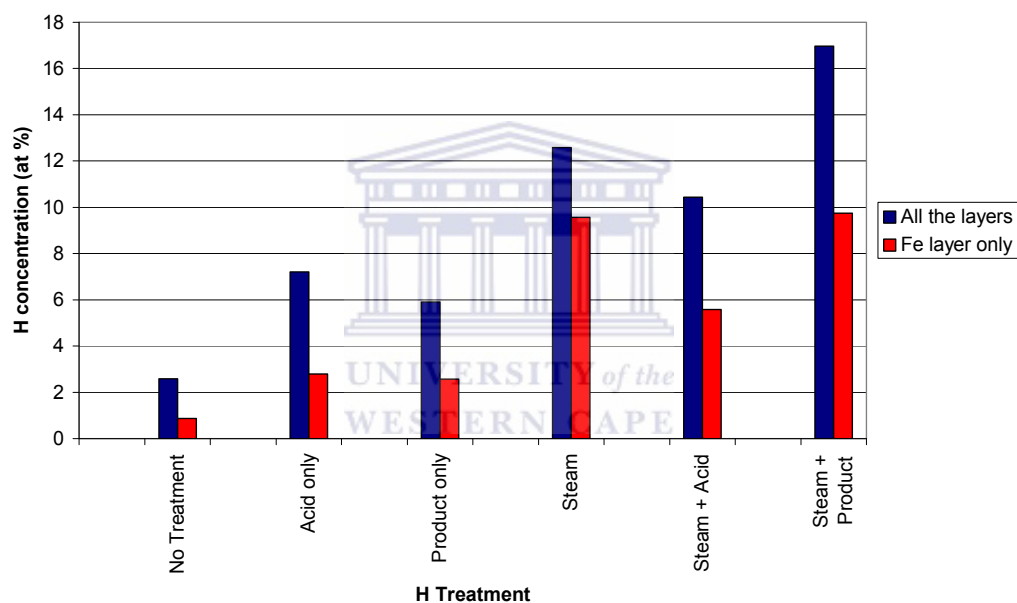


**Figure 5-10: Quantitative analysis of the average hydrogen concentrations for different H treatments.**

Based on the above figure, any of the treatments would cause H to diffuse into the unprotected tinplate samples. Even if the samples were exposed to acid or product without steam, some hydrogen uptake would occur throughout the samples. When the unprotected samples were exposed to steam, whether it is with acid or fish severe hydrogen uptake occurred throughout the samples.

## Results and Discussion

This confirms the fact that the exhaust box would cause severe H uptake to the unprotected cans. This damage refers to hydrogen uptake and the effects of hydrogen uptake in metals. This is not the case in factories though; all cans are protected inside and outside. In the next section the samples will be prepared with all the protection on the samples.

The second set of comparisons will now follow:

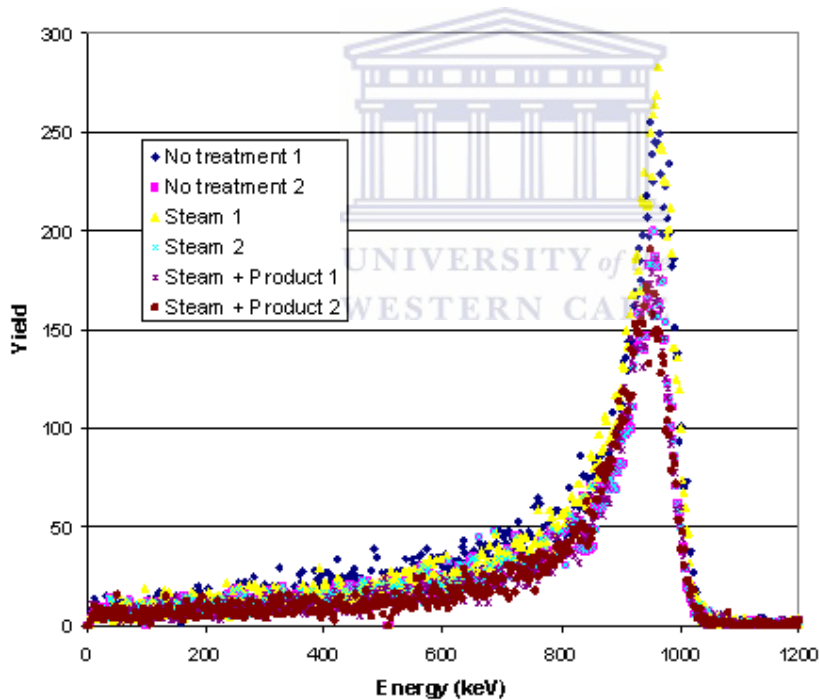


**Figure 5-11: A comparison of the ERDA spectra for differently prepared samples protected with lacquer protection.**

According to the spectra all the samples behaved the same. Some minor differences occurred at the surface in terms of hydrogen concentration, but they all definitely overlap. Compared to the spectra for unprotected samples



all these samples displayed no differences. This means the can that was sent through the exhaust box was exactly the same as the can that was still in the crates before it went through. The exhaust box does not affect the cans in terms of hydrogen uptake. Hydrogen did not diffuse into the metal matrix when the tinplate had the lacquer protection.

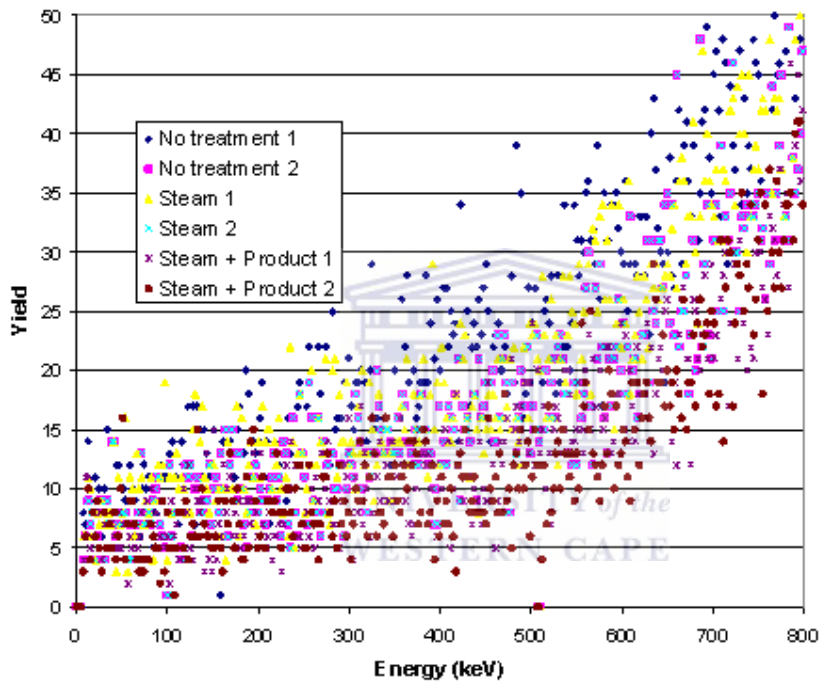


Figure 5-12: A close up ERDA spectrum of the comparison for differently prepared samples

By taking a closer look at the spectrum above it is difficult to distinguish which graph is higher or lower. This confirms that the  $H^+$  concentration of all the samples were similar. This also confirms that the  $H^+$  concentration for the untreated samples were the same as the treated samples. Therefore no  $H^+$  diffused into the material.

## Results and Discussion

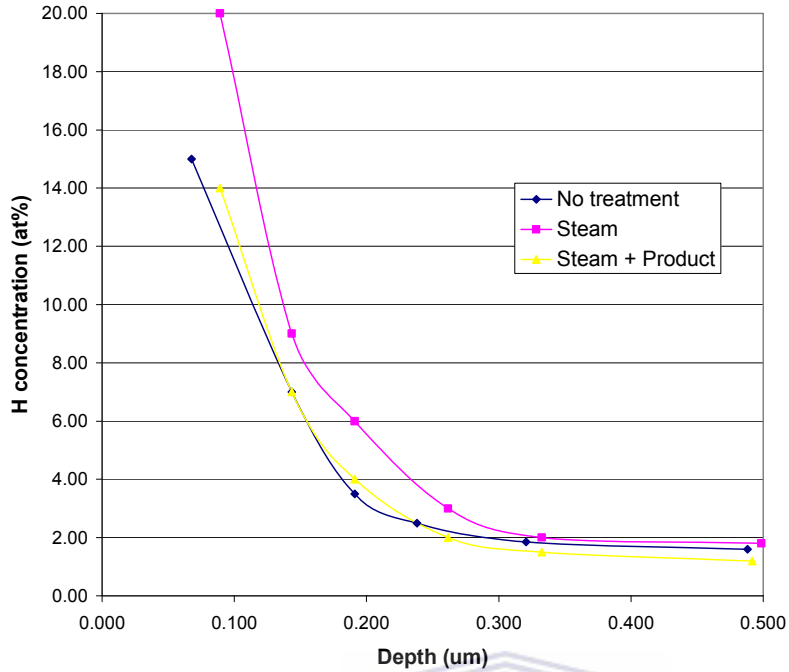


Figure 5-13: A depth profiling curve for differently prepared samples with lacquer protection.

The concentration of H throughout the sample and the concentration of H in the Steel matrix are shown below:

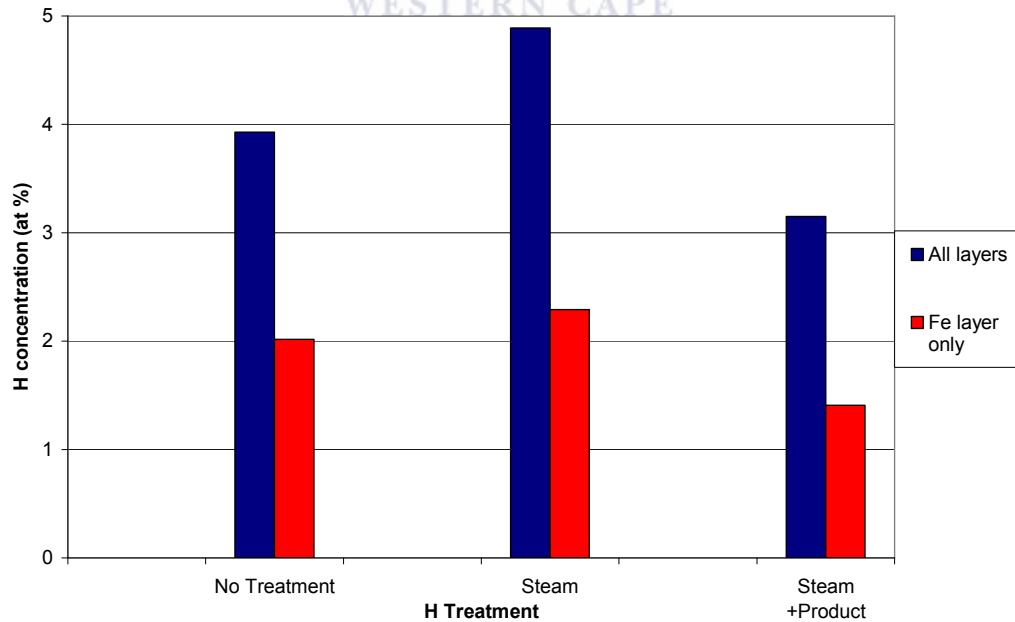


Figure 5-14: A quantitative analysis of the hydrogen concentration throughout the sample and in the steel matrix of the protected samples.

Based on the figure above the hydrogen concentration throughout the protected samples are consistent to within 2 at%. And the hydrogen concentration in the steel matrix is consistent to within 0.5 at%. Compared to the unprotected samples all these samples had the same hydrogen concentration. Based on the above figure it is safe to say that the steam or the steam together with the product did not affect the protected samples.

### ***5.2) Residual Stress Analysis***

For this set of analysis the samples were prepared as in the second set of samples prepared for ERDA. The cans were sent through their respective treatments then put in to XRD machine. The whole can was put into the machine due to the fact that the metal would relax if the can was cut.

The tinfoil sample consists of many layers as discussed above. The only layer that could cause the can to fail is the Fe layer. The residual stress was measured in the Fe layer.

The first step was to check if the X-ray beam would penetrate all the surface layers. Phase analysis was done on a piece of tinfoil and peaks for all the layers were shown. The phase analysis was done at iThemba LABS in Cape Town.

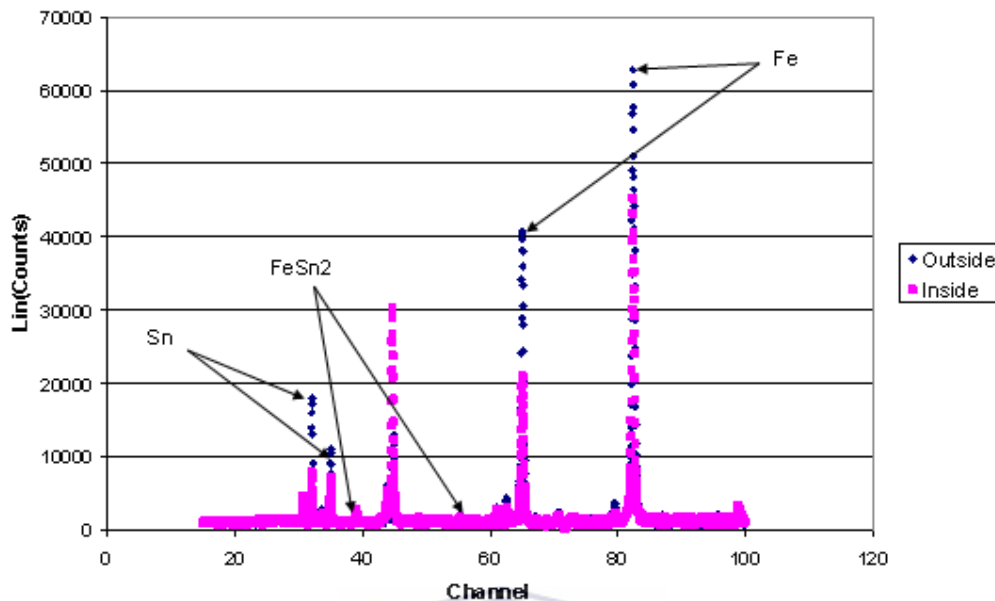


Figure 5-15: Phase Analysis for a tinplate sample.

The sample was analysed on the inside and the outside of the can. The protective layer on the inside is thicker than the layer on the outside. It can clearly be seen by the difference in the number of counts. The peaks for the Fe layers were very clear. So it was assumed that the stress analysis in the Fe layer wouldn't be a problem.

The residual stress analysis at NECSA was done using 2-dimensional x-ray diffraction. The (310) plane of the Fe layer was analysed with 0.154055nm Cu radiation at a  $2\theta$  peak position  $116^\circ$ . The Poisson ratio was 0.32 and Young's Modulus was 181159 N.m. The (220) plane of the Fe layer was also analysed with 0.178897nm Co radiation at a  $2\theta$  peak position  $123^\circ$ . The Poisson ratio was 0.28 and Young's Modulus was 220264.00 N.m.

The samples were tilted in many different ways. The sample was tilted in 6 different phi directions. For each phi tilt the sample was tilted another 7 different omega directions. The sample was tilted in 35 different directions to produce a good estimate of the residual stress.

The data collected by a 2 dimensional detector were not a spectrum but as follows:

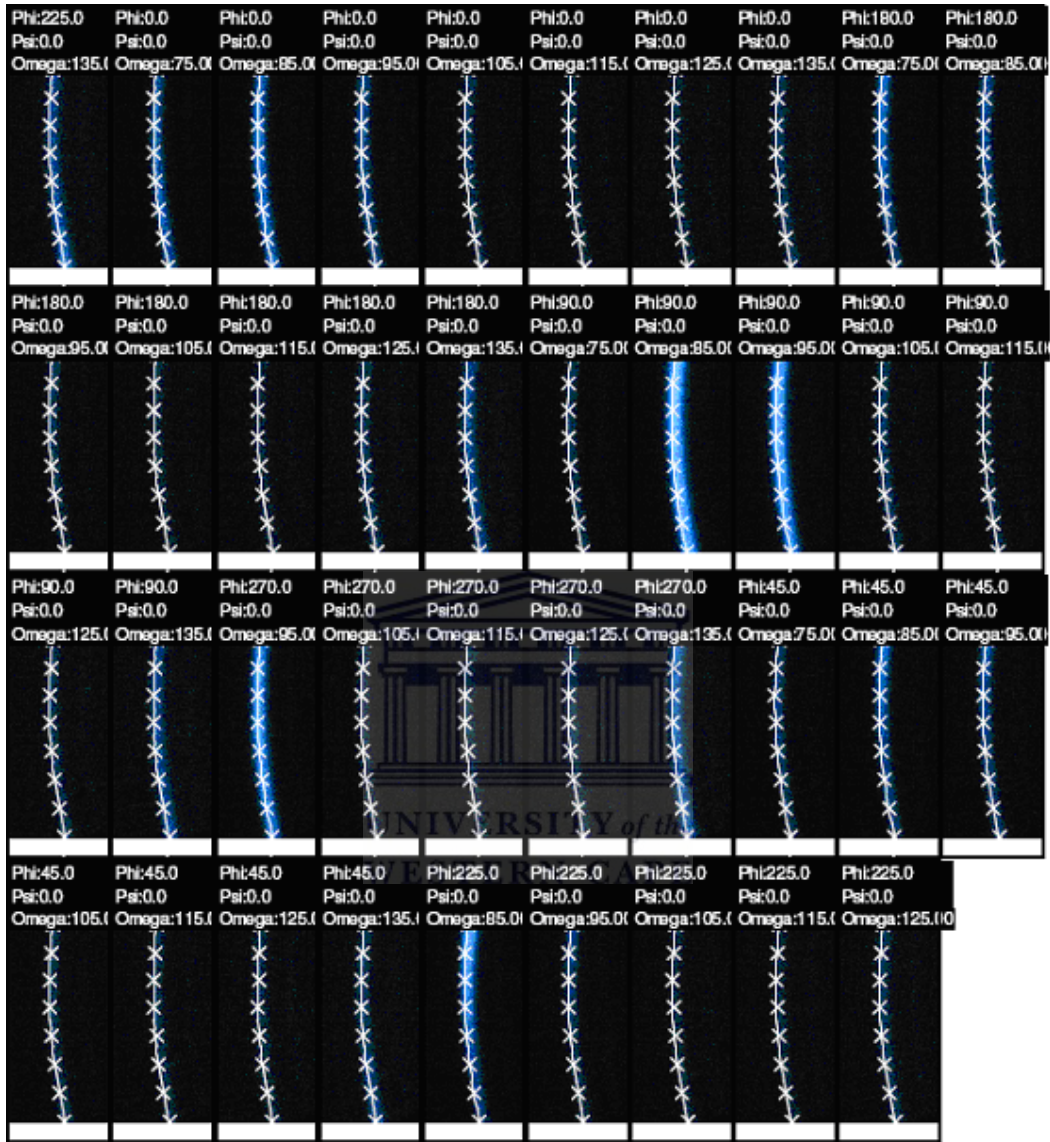


Figure 5-16: Images of the diffracted beam at different sample tilts for 2D XRD.

The Pearson VII Peak Evaluation Method (PEM) and the triaxial stress model were used to analyse the above data. When the data were analysed a stress tensor in the form of a 3 by 3 matrix was produced.

## Results and Discussion

A typical Stress Tensor:

$$\begin{pmatrix} -539.0 \pm 189.7 & -107.6 \pm 83.7 & -25.20 \pm 22.6 \\ -107.6 \pm 83.7 & -824.7 \pm 222.6 & -83.60 \pm 26.4 \\ -25.2 \pm 22.6 & 83.60 \pm 26.4 & -105.6 \pm 104.8 \end{pmatrix}$$

This matrix can be manipulated so that all the shear components are removed. The result is called the principle stress tensor:

$$\begin{pmatrix} -867.4 & 0 & 0 \\ 0 & -509.2 & 0 \\ 0 & 0 & -92.8 \end{pmatrix}$$

The  $d_0$  was calculated using the software to be 0.0905nm.

The first set of cans were measured with a Cu tube and the second set were measured with a Cr tube. The principle stress tensors will be compared for each can. 3 similar cans went through the same treatment. The cans were only treated with steam and steam + product and were compared to untreated cans. In total 9 cans were used.

**Table 5-4: Residual Stress data for 3 different stress orientations and all the respective treatments using the Cu tube.**

H Treatment	$\sigma_1$ (MPa)	$\sigma_2$ (MPa)	$\sigma_3$ (MPa)
No Treatment 1	-424.4	-229.7	29.6
No Treatment 2	448.8	221.5	4.2
No Treatment 3	-311.8	-110.3	0.7
Steam 1	-867.4	-509.2	-92.8
Steam 2	-868.3	-241	48.3
Steam 3	-340	-107.3	0.6
Steam + Fish 1	-1015.5	-523.6	-105.7
Steam + Fish 2	-281.0	-172.6	25.1
Steam + Fish 3	-284.3	-125.8	15.0

Table 5-5: Average Residual Stresses measured with the Cu tube for the respective treatments.

H Treatment		$\sigma_1$ (MPa)	$\sigma_2$ (MPa)	$\sigma_3$ (MPa)
No H treatment	Average Stress	-95.8	-39.5	11.5
	Standard Dev.	475.0	233.8	15.8
Steam	Average Stress	-691.9	-285.8	-14.6
	Standard Dev.	304.8	204.7	71.8
Steam + Product	Average Stress	-526.9	-274.0	-21.9
	Standard Dev.	423.1	217.4	72.8

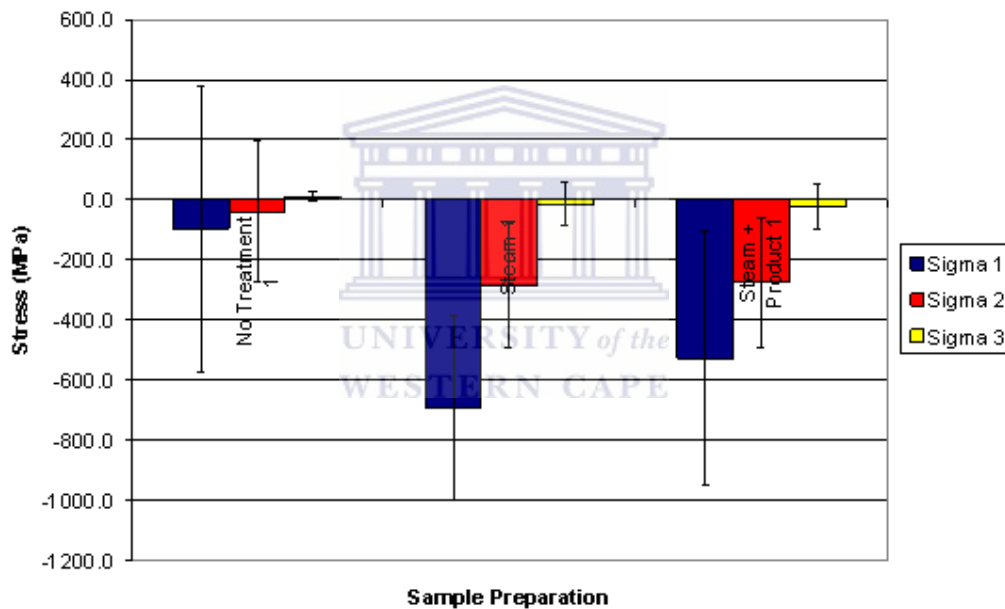


Figure 5-17: Average Residual Stress measurements for the respective treatments with a Cu tube.

The reason for measuring the residual stress was to check if any hydrogen penetrating into the steel matrix caused some distortion between the atomic lattice planes.

All the results for  $\sigma_3$  are close to 0 MPa. The results for  $\sigma_1$  and  $\sigma_2$  were both in compression. Metals split when they are in tension and not in compression. The stress orientation of concern was  $\sigma_1$  because the cans split along the circumference of the can. The results showed that the material was

## Results and Discussion

compressive in the  $\sigma_1$  stress but had a data variation of 1000 MPa which was not acceptable. The material was also in a compressive stress state in the  $\sigma_2$  direction but also had a data variation of 600 MPa. These results were not acceptable because any difference in residual stress would not be detected.

If the results were to be accepted the samples had a higher surface compression which is good for the can. This was the opposite effect of hydrogen embrittlement. Based on the above results for residual stress, when the samples were treated the stress state was improved.

The measurements were repeated with a Co tube. This was done after comparing the signal to noise ratios of Co to Cu. The following data displayed the peaks above background:

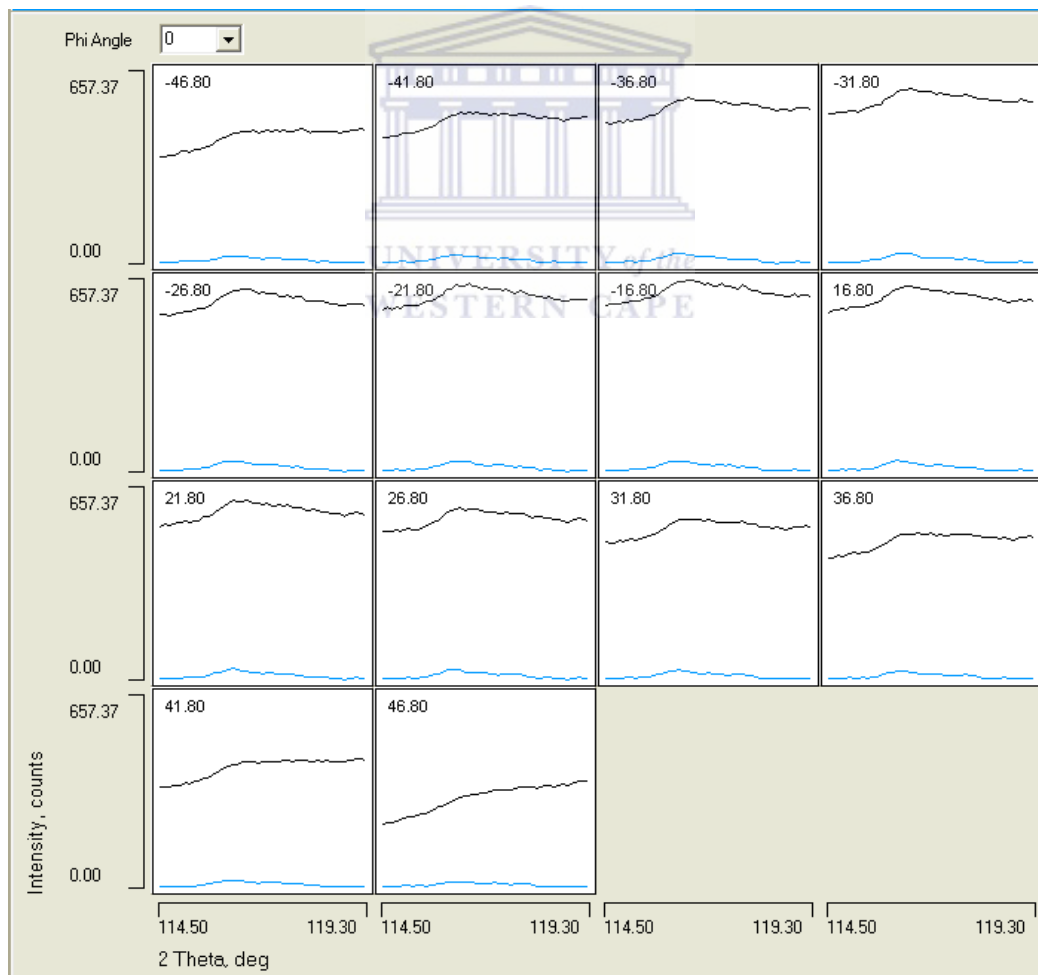
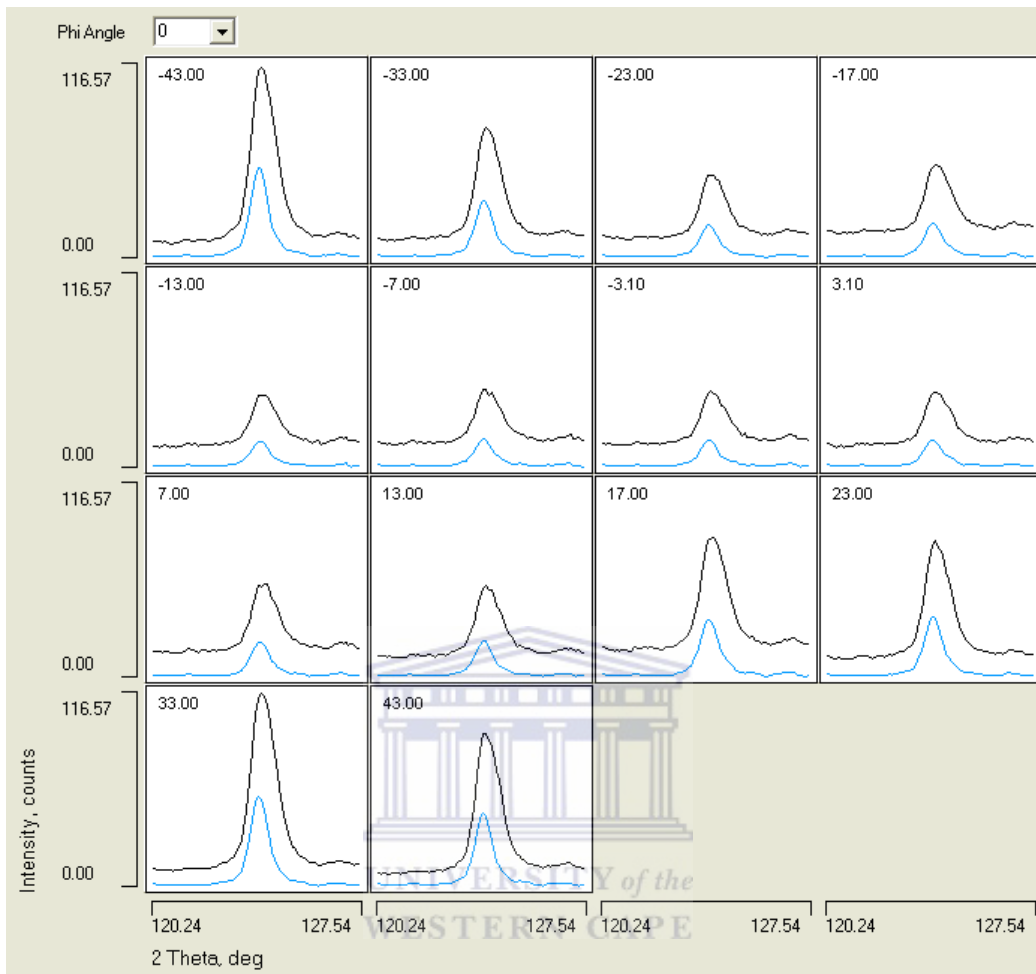


Figure 5-18: The signal to noise ratio for the Cu tube.





**Figure 5-19: The signal to noise ratio for the Co tube.**

The black graph displays the raw data and the blue graph displays the processed data. The data was processed with the software by smoothing the data and removing the background. The graphs for the Cu tube displays a very high background and the graphs for the Co tube displays very nice peaks above background, bearing in mind that the background is being subtracted. When looking at the graphs produced with the Cu tube the peak is not very visible and it looks like there is a little shoulder present as well. These are a few factors of concern when doing stress analysis and can affect the results if the wrong tube is used. When looking at the graphs produced by the Co tube the peaks are very clear and no shoulder is present. The above two figure

makes it very clear that the results produced with the Co tube is much more reliable than those of the Cu tube.

**Table 5-6: Residual Stress data for 3 different stress orientations and all the respective treatments with the Co tube.**

H Treatment	$\sigma_1$ (MPa)	$\sigma_2$ (MPa)	$\sigma_3$ (MPa)
No Treatment 1	136	46.8	-0.5
No Treatment 2	74.3	-21.8	0.1
No Treatment 3	56.8	20.7	-2
No Treatment 4	71	-15.7	1.7
Steam 1	86.8	35.9	-0.4
Steam 2	95.4	-11.6	2.7
Steam 3	84.6	22.6	-2.5
Steam 4	58.7	-28.1	1.6
Steam + Fish 1	53	-36.5	-0.6
Steam + Fish 2	75.2	-28.3	-0.1
Steam + Fish 3	34.5	26.7	10.9
Steam + Fish 4	98.4	-16	-0.1

UNIVERSITY of the  
WESTERN CAPE

**Table 5-7: Average Residual Stress measurements for the respective treatments with the Co tube.**

H Treatment		$\sigma_1$ (MPa)	$\sigma_2$ (Mpa)	$\sigma_3$ (Mpa)
No H treatment	Average Stress	84.53	7.50	-0.18
	Standard Dev.	35.15	32.23	1.53
Steam	Average Stress	81.38	4.70	0.35
	Standard Dev.	15.82	29.64	2.29
Steam + Fish	Average Stress	65.28	-13.53	2.53
	Standard Dev.	27.65	28.11	5.59

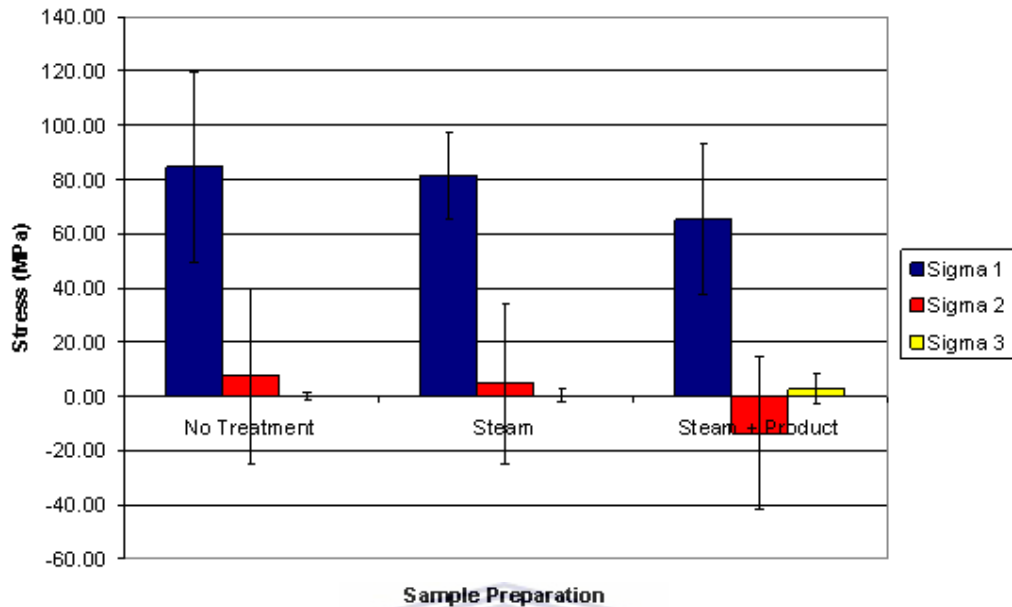


**Figure 5-20: Average Residual Stress measurements for the respective treatments using the Co tube.**

The solid bar graph indicates the average stress in its particular stress orientation. The error bars displays the data variation for the 4 cans prepared similarly.

In the  $\sigma_1$  stress orientation the samples had an average residual stress of 80 MPa and a data variation of 70 Mpa. As the sample was treated with steam and steam with product, the  $\sigma_1$  stress state of the metal was improved slightly. The samples were in a tensile state which was of concern but when compared to the ultimate tensile strength of 700 MPa, the residual stress was negligible.

In the  $\sigma_2$  stress orientation the samples had an average residual stress of 5 MPa and a data variation of 60 MPa. As the sample was treated the stress state in the  $\sigma_2$  direction also improved by a minimal amount.

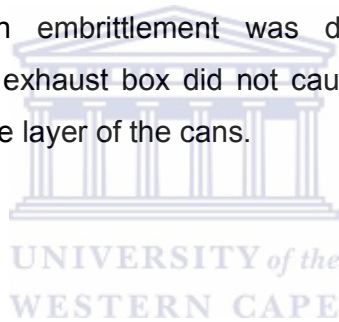
In the  $\sigma_3$  stress orientation the samples had an average residual stress of 0 MPa and a data variation of 5 MPa. As the sample was treated with steam the

## Results and Discussion

stress state remained the same and when the sample was treated with steam and product the stress state in the  $\sigma_3$  direction degraded by a minimal amount.

In summary none of the stress values were exactly the same when the samples were prepared similarly. This was the case for treated and untreated samples. All the samples had the same data variation and this meant that no can would be in a single stress state. Each sample preparation had a range of stresses and no significant changes were observed when the samples were treated compared to the untreated samples.

Since the residual stresses of the treated samples were the same as the untreated samples, the steam or the product does not affect the can in anyway. And no distortion between atomic planes was observed; hence no observation of hydrogen embrittlement was detected using 2D x-ray diffraction. Therefore the exhaust box did not cause any distortion between the atomic planes in the Fe layer of the cans.



## Tensile Testing

Table 5-8: Samples with no treatment.

Sample Name	Load at Offset Yield (kN)	Stress at offset Yield (Mpa)	Load at Max Load (kN)	Stress at Max Load (Mpa)	Maximum Diasplacement (mm)	Maximum Percent Strain (%)
1	1.531	814.002	1.534	815.667	0.931	1.862
2	1.443	759.176	1.558	819.707	0.353	0.707
3	1.035	586.483	1.325	750.891	0.409	0.819
4	1.491	769.966	1.522	785.832	0.244	0.488
5	1.393	821.965	1.393	821.800	0.204	0.409
Mean	1.379	<b>750.318</b>	1.466	<b>798.779</b>	0.428	0.857
S.D	0.199	<b>95.519</b>	0.102	<b>30.471</b>	0.293	0.585
Minimum	1.035	586.483	1.325	750.891	0.204	0.409
Max	1.531	821.965	1.558	821.800	0.931	1.862

Table 5-9: Samples exposed to steam only

Sample Name	Load at Offset Yield (kN)	Stress at offset Yield (Mpa)	Load at Max Load (kN)	Stress at Max Load (Mpa)	Maximum Diasplacement (mm)	Maximum Percent Strain (%)
1	1.506	840.030	1.544	861.203	0.262	0.524
2	1.511	805.079	1.544	822.808	0.252	0.505
3	1.007	559.096	1.542	855.811	0.617	1.234
4	1.198	617.353	1.221	629.216	0.267	0.534
5	1.383	746.202	1.552	837.253	0.384	0.767
Mean	1.321	<b>713.552</b>	1.481	<b>801.258</b>	0.356	0.713
S.D	0.217	<b>120.986</b>	0.145	<b>97.375</b>	0.155	0.310
Minimum	1.007	559.096	1.221	629.216	0.252	0.505
Max	1.511	840.030	1.552	861.203	0.617	1.234

Results and Discussion

Table 5-10: Samples exposed to Steam + Fish

Sample Name	Load at Offset Yield (kN)	Stress at offset Yield (Mpa)	Load at Max Load (kN)	Stress at Max Load (Mpa)	Maximum Diasplacement (mm)	Maximum Percent Strain (%)
1	1.476	795.716	1.493	804.973	0.833	1.666
2	1.338	748.106	1.338	747.967	0.219	0.437
3	1.424	714.466	1.572	788.634	0.339	0.677
4	1.192	628.793	1.358	716.396	0.376	0.753
5	1.624	847.868	1.624	847.785	0.275	0.550
Mean	1.411	<b>746.990</b>	1.477	<b>781.151</b>	0.408	0.817
S.D	0.161	<b>83.036</b>	0.127	<b>50.887</b>	0.245	0.490
Minimum	1.192	628.793	1.338	716.396	0.219	0.437
Max	1.624	847.868	1.624	847.785	0.833	1.666

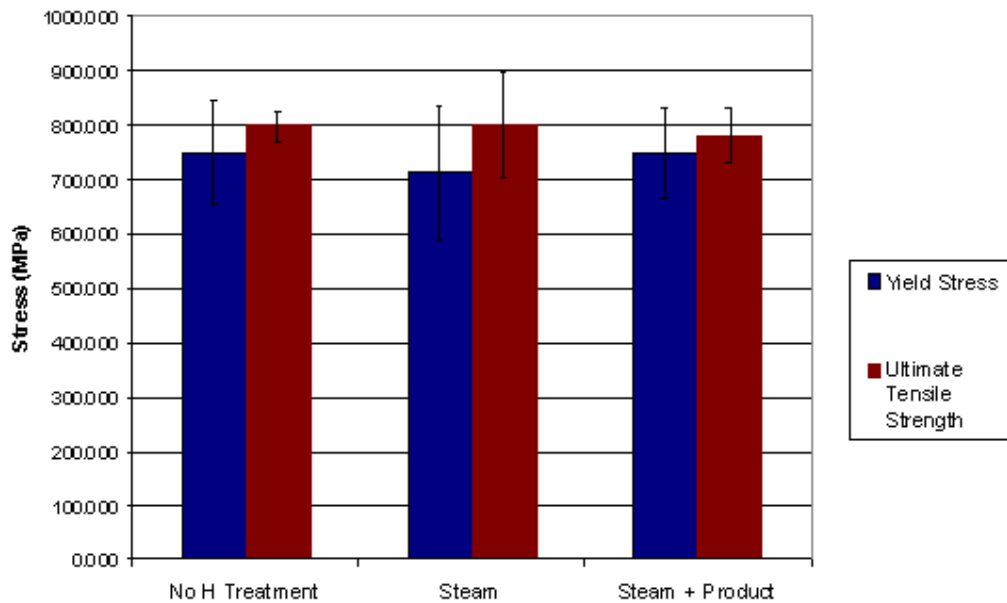


Figure 5-21: Average tensile stresses for differently prepared samples.

The tensile tests were performed to check if the available diffused hydrogen or the heat process produced by the exhaust box reduced the yield stress of the steel in the cans. Based on the above figure, all the yield strengths and the ultimate tensile strengths were the same within the error bars displayed. This means the hydrogen treatments and the heat process produced in the exhaust did not affect the strength of the metal in the cans.

The results above was the best produced out of many trials. The problems encountered were due to the complex structure of the tinplate sample. The sample was multilayered, curved and very corrosive in atmospheric conditions.

Sample preparation for ERDA was very complicated. When the lacquer and the tin layers were removed the sample corroded within five minutes. The last trial was done with the last tin protection layer present to prevent the corrosion.

For XRD, mounting a can turned out to be very time consuming since the machine was built to suit flat and tiny samples. Cutting the cans would cause them to relax in terms of stress and would produce unreliable results. The fact that the samples had many layers was a problem as well and the size of the samples sometimes caused shading to the detector affecting the results.

For tensile testing, technical aspects were encountered like a non homogeneous thickness of the sample, the sample was very thin for sample preparation, i.e. during machining, and the software only accommodated built in functions for tinplate sheets not cans.

The above mentioned problems were a few out of many that were encountered and solved during the measurements taken with the mentioned techniques used. Planning any kind of work on hydrogen embrittlement or corrosion was quite difficult. Research was done in this field of science with results and theories contradicting each other.

## Results and Discussion

In the end a good literature review was done together with the best equipment available in South Africa for measurements. The results could not be compared to previous measurements done by other research, since tinplate was not measured with the equipment mentioned above. The theories put forward and the discussions were logical.





## CONCLUSION

Many theories have been put forward as to why H embrittlement caused metals to fail. These theories were put to test to check if H embrittlement contributed towards the formation of split bodies/flanges in the cans due to the exhaust box. When the theories were put to test, no indication of H embrittlement was displayed.

Based on the ERDA results a simulation of potential hydrogen embrittlement occurred when tinplate cans without any lacquer was sent through the exhaust box. When the real case fish factory scenario was simulated no indication of H embrittlement was present in the protected cans. The results really displayed the benefit of the lacquer in 2-piece cans.

The residual stress showed no indication of planes being distorted and hence no hydrogen embrittlement either. The results also proved that the Co tube produced better results than the Cu tube. It only confirmed the good state of the metal. The tensile strengths displayed no differences when the samples were exposed to the various hydrogen treatments. The tensile tests confirmed that the steam did not reduce the strength of the metal.

After all the results and the discussions displayed above no indication of hydrogen embrittlement was found present. If the exhaust box was the reason the cans failed, hydrogen embrittlement was not the cause.

## REFERENCE

- [1.1] Barritt, A.S. (1994). Detection of Hydrogen Embrittlement in steel and steel alloys using methods of neutron radiography. Massachusetts Institute of Technology. Cambridge.
- [2.1] Davis, R. (2008). Tinsplate in the canning industry. Nampak R&D. South Africa
- [3.1] A Climent-Font, U Watjen, H Bax. Quantitative RBS analysis using RUMP on the accuracy of the He stopping in Si. Nucl. Instr. and Meth. B71 (1992) 81
- [3.2] R Behrisch, S Grigull, U Kreissig, R Grotzschel. Influence of surface roughness on measuring depth profiles and the total amount of implanted ions by RBS and ERDA, Nucl. Instr. and Meth. B 136-138 (1998) 628-632
- [3.3] A Coban, M.M. Khaled. Analysis of hydrogen in corrosion product films on molybdenum and niobium using ERDA technique, International Journal of Hydrogen energy 24 (1999) 1101-1105
- [3.4] Ali Coban, M.M. Khaled. Analysis of hydrogen in corrosion product films on molybdenum and niobium using ERDA technique. International Journal of Hydrogen Energy 24 (1999) 1101-1105
- [3.5] Maas, A.J.H. Elastic Recoil Detection Analysis with  $\alpha$ -particles, Eindhoven University of Technology, 1998.
- [3.6] L C Feldman, J W Mayer. Fundamentals of surface and thin films analysis, North Holland Amsterdam, 1986.

[3.7] W M Arnold Bik, F H P M Habraken. Elastic Recoil Detection, Phys. 56 (1993) 859-902

[3.8] N Bohr. Mat. Fys, Medd. Dan. Vid. Selsk. 18 (8) (1948).

[3.9] M. Mayer. *SIMNRA User's Guide*, Report IPP 9/113, Max-Planck-Institut für Plasmaphysik, Garching, Germany, 1997

[3.10] Anderoglu O, (2004). Residual Stress Measurement using x-ray diffraction. A&M University. Texas.

[3.11] Noyan IC, Cohen JB. Residual Stress Measurement by Diffraction and Interpretation, New York: Springer-Verlag; 1987.

[3.12] Bruker advanced x-ray solutions, Introduction to 2D XRD training manuel, Madison, Wisconsin, USA, 2002

